Yan, Q., Wu, X., Yuan, X., & Geng, Y. (2016). An Improved Grid Voltage Feedforward Strategy for High-Power Three-Phase Grid-Connected Inverters based on the Simplified Repetitive Predictor. IEEE Transactions on Power Electronics, 31(5), 3880-3897. DOI: 10.1109/TPEL.2015.2461632

Peer reviewed version

An Improved Grid Voltage Feedforward Strategy for High-Power Three-Phase Grid-Connected Inverters based on the Simplified Repetitive Predictor

Qingzeng Yan, Xiaojie Wu, *Member, IEEE,* Xibo Yuan, *Member, IEEE,* and Yiwen Geng

***Abstract*—When faced with distorted grid voltage, more harmonics will appear in the output currents of the grid-connected inverters. The grid voltage feedforward strategy, as the most direct solution to compensate the harmonics, however, is seriously affected by the errors in the grid voltage feedforward loop, such as delays. This issue is more significant for high power inverters where the switching frequency is relatively low (<5kHz), and the grid-interface inductance is small (<0.5mH). The errors mainly include the signal distortion caused by the conditioning circuits, the control delay of the digital controller, and the zero-order hold (ZOH) characteristic of pulse width modulation (PWM). In this paper, several improvements have been made to reduce the signal distortion and compensate the delays. A second-order Butterworth low-pass filter in the conditioning circuit is carefully designed with the maximum flat magnitude response and the almost linear phase response to avoid distorting the measured grid voltage. Further, based on the conventional repetitive predictor, an open-loop simplified repetitive predictor is proposed to compensate the delays in the grid voltage feedforward loop. Three predictive steps are achieved by the open-loop simplified repetitive predictor to compensate the delays: one step for the delay caused by the conditioning circuit, the second step for the control delay of the digital controller, and the third step for the ZOH characteristic of PWM. The effectiveness of the improved grid voltage feedforward strategy are experimentally validated on a 250kVA solar power generation system, where the current harmonics are effectively attenuated. In addition, the inverter starting current is suppressed.**

***Index Terms*—Delay compensation, distorted grid voltage, grid voltage feedforward, open-loop simplified repetitive predictor, three-phase grid-connected inverters.**

I. Introduction

Nowadays, nonlinear loads based on power electronic converters are widely used, which introduces harmonic distortion in the grid voltage especially when the grid is not strong enough (weak or remote systems) [1], [2]. Although the IEEE standard 1547-2003 has defined the total harmonic distortion (THD) of the grid voltage to be below 5.0%, the grid-connected inverters, especially high power inverters with relatively low switching frequency and small filtering inductance, are seriously affected by the grid voltage distortion, resulting in more harmonics in the output current. Furthermore, if a large amount of current harmonics are injected into the grid, the grid voltage distortion will be further intensified [1]. As a key equipment in renewable power generation systems, the grid-connected inverters must be optimized to cope with the voltage harmonics.

There are many factors contributing to the output current harmonics of grid-connected inverters, such as grid voltage distortion, sampling precision and other factors as detailed in Fig. 1, where this paper will focus on the compensation of grid voltage distortion (harmonics). The current harmonics can be divided into high-frequency (switching frequency) harmonics and low-frequency (multiples of fundamental frequency) harmonics. The high-frequency current harmonics caused by the device switching can be effectively minimized by the output filters, e.g. *L* or *LCL* filters. The low-frequency current harmonics, however, if attenuated by passive output filters, the filters will be bulky and costly [3]. Hence, using control strategies to attenuate the low-frequency current harmonics is a method widely adopted.

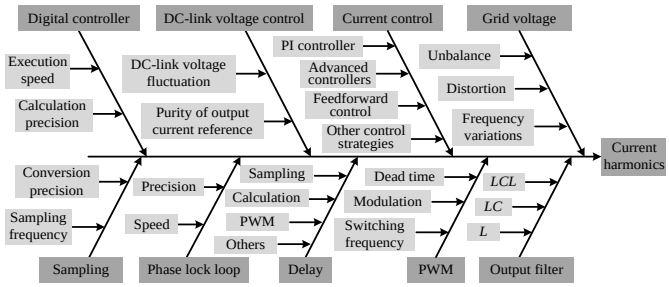

Fig. 1. Factors contributing to the output current harmonics of grid-connected inverters.

There have already been several methods to attenuate the low-frequency current harmonics due to the grid voltage harmonic distortion. They can be grouped into two categories: methods using special current controllers to obtain high gains at harmonic frequencies, and methods feeding forward specific terms to the control loop. For the conventional inverters controlled in the synchronous frame with proportional-integral (PI) controllers, simply increasing the proportional or integral gain can attenuate the output current harmonics to some extent. However, the cost is the reduced stability and noise immunity of the system [3], [4]. In [5], several PI controllers are adopted based on multiple synchronous frames to attenuate each

This work was supported in part by the National Natural Science Foundation of China under Project 51377160 and the Newton Research Collaboration Programme under Project NRCP/1415/138.

Q. Yan is with the School of Information and Electrical Engineering, China University of Mining and Technology, Xuzhou, Jiangsu 221116, China, and also with the Department of Electrical and Electronic Engineering, University of Bristol, Bristol BS8 1UB, U.K. (e-mail: yqz2009@163.com).

X. Wu and Y. Geng are with the School of Information and Electrical Engineering, China University of Mining and Technology, Xuzhou, Jiangsu 221116, China (e-mail: zgcumt@126.com; gengyw556@126.com) (Corresponding author: X. Wu).

X. Yuan is with the Department of Electrical and Electronic Engineering, University of Bristol, Bristol BS8 1UB, U.K. (e-mail: xibo.yuan@bristol.ac.uk).

individual harmonics and the computational burden is significant. Given PI controllers' drawback of low gains at harmonic frequencies, alternatively, controllers such as resonant (R) controllers [6] and vector-proportional-integral (VPI) controllers [7], [8] can be adopted, which have extremely high gain at their resonant frequencies. In combination with the proportional controller or PI controller, further PR controllers [9], PI-R controllers [10] and PI-VPI controllers [11] are proposed, where good current harmonics minimization capability, as well as satisfying dynamic and steady-state performance can be obtained. However, with one resonant or VPI controller, only a pair of negative and positive harmonic components can be regulated. If several current harmonic components need to be eliminated, more controllers should be added, which increases the complexity of the control system [12]. Further, the system becomes unstable if the resonant frequencies of the added resonant controllers are outside the bandwidth of the current control loop [2], [8]. Several literatures have proved that the repetitive controller serves as a bank of resonant controllers, and it is capable of regulating a series of harmonic components [13], [14]. However, the repetitive controller deeply relies on the former input values, which limits the dynamic response of the current control loop.

Feedforward methods have been widely used in control applications to lower the output current harmonics and increase the dynamic response of the system [15]-[24]. The proportional feedforward of the output currents [15]-[17] can only compensate the current harmonics caused by nonlinear loads, but incapable of suppressing the current harmonics caused by the grid voltage distortion. With the aim of suppressing the impact of the distorted grid voltage, the grid voltage feedforward strategy is the most direct solution which incorporates the measured grid voltage in the control loop through an additional feedforward path. The grid voltage full-feedforward strategy for single-phase *LCL* based grid-connected inverters is proposed in [18] dealing with the distorted grid voltage conditions. [19] and [20] extend the grid voltage full-feedforward strategy to the three-phase inverters. Besides the grid voltage, the full-feedforward strategy also requires the feedforward of another two derivative terms, which are sensitive to high-frequency noises, making it hard for practical implementation [21], [22]. As a further extension, an improved grid-voltage estimator is proposed in [21] to solve this derivative problem. But the errors in the feedforward loop, which affect the feedforward precision, are still not addressed in detail. Theoretically, the simple proportional grid-voltage feedforward strategy can effectively suppress the impact of the distorted grid voltage on the system. However in practice, due to the lack of feedforward precision, the grid voltage feedforward term cannot sufficiently cancel the distorted grid voltage leading to a non-ideal performance. Regarding the grid voltage feedforward strategy adopted in [23], only one control step is predicted by the consecutive voltage samples, and in [24], only the delay caused by the conditioning circuits is considered, which will limit the capability of cancelling the harmonics in grid voltage. There is lack of systematic analysis of how various factors, e.g. sampling errors, control delay, and the zero-order hold (ZOH) characteristic of pulse width modulation (PWM), affect the grid voltage feedforward strategy. While these factors may be acceptable for high-switching-frequency low-power systems, it can however be a serious issue for high-power systems with low-switching-frequency (<5kHz) and low inductance (<0.5mH).

In this paper, the study of how to lower the current harmonics with the distorted grid voltage is based on the conventional grid voltage feedforward strategy. The errors in the feedforward loop which affect the performance of the conventional grid voltage feedforward strategy are investigated in detail, drawing to the conclusion that the errors in the feedforward loop mainly include the signal distortion caused by the conditioning circuit, the control delay of the digital controller, and the ZOH characteristic of PWM.

The amplitude errors of the grid voltage feedforward loop can be adjusted by regulating the gain of feedforward loop. However, the compensation of the phase delay of the feedforward voltage is challenging. Since the fundamental and harmonic components of the grid voltage are repetitive every cycle when the grid is stable, the repetitive predictor [25]-[27] is adopted in this paper to compensate the delays in the grid voltage feedforward loop. And based on the conventional closed-loop repetitive predictor [25], an open-loop simplified repetitive predictor is proposed with reduced computational and design complexity, and the elimination of stability issues. Considering the limited dynamic response of the repetitive predictor, the hysteresis error of the open-loop simplified repetitive predictor is analyzed and presented in this paper.

In the grid voltage feedforward loop, the commonly used 2nd order Butterworth low-pass filter [28], [29] in the conditioning circuit may distort the measured grid voltage and degrade the feedforward performance. Meanwhile, the open-loop simplified repetitive predictor implemented by the digital controller can only predict the signal certain steps ahead, i.e. the predictor has a linear phase characteristic. To cooperate with the linear phase characteristic of the repetitive predictor and enhance the grid voltage feedforward performance, the 2nd order Butterworth low-pass filter is carefully designed with the maximally flat magnitude response and the almost linear phase response. With the designed 2nd order Butterworth low-pass filter and the open-loop simplified repetitive predictor, the delay in the feedforward loop is compensated effectively. Further, the delay-compensation states indicated by the harmonic admittances have been classified into three cases: the partial compensation state, the full compensation state, and the over compensation state.

This paper is structured as follows. In Section II, the errors between the digital controller and the power circuit of the inverter systems are listed and analyzed. Section III analytically derives the impact of the errors in feedforward loop on the grid voltage feedforward strategy. Then, an open-loop simplified repetitive predictor is proposed with its hysteresis error derived numerically in Section IV. The conditioning circuit is carefully designed in Section V to obtain the maximally flat magnitude response and the almost linear phase response. In Section VI, using the improved grid voltage feedforward strategy based on the simplified repetitive predictor, with the delays in the current loop considered, the current control loop is designed and the delay-compensation states of the grid voltage feedforward loop are classified. Lastly, the correctness of the analysis and the effectiveness of the improved grid voltage feedforward strategy are experimentally validated on a 250kVA solar power generation system in Section VII.

II. Errors between the Digital Controller and the Power Circuit of the Inverter Systems

The diagram of a three-phase transformerless grid-connected photovoltaic (PV) inverters is shown in Fig. 2. L_1, L_2, R_f and C_f are the inverter-side inductance, the grid-side inductance, the damping resistance, and the capacitance of the *LCL* filter, respectively. And C_{dc} is the dc-link capacitance.

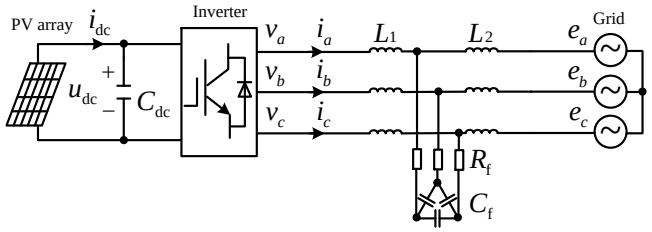

Fig. 2. Power circuit of three-phase tansformerless grid-connected PV inverters.

For the convenience of later analysis, the mathematical model of the PV inverter system is derived in the synchronous rotating (*d*-*q*) coordinate. Given the well-damped *LCL* filter in Fig. 2 can be treated as an equivalent *L* filter at low frequencies [30], the average mathematical model for voltage and power can be expressed as [31]-[33]

$$\begin{bmatrix} v_d \\ v_q \end{bmatrix} = \begin{bmatrix} Ls+R & -\omega_1 L \\ \omega_1 L & Ls+R \end{bmatrix} \begin{bmatrix} i_d \\ i_q \end{bmatrix} + \begin{bmatrix} e_d \\ e_q \end{bmatrix}, \tag{1}$$

$$\frac{3}{2}(v_d i_d + v_q i_q) = u_{dc} i_{dc} \tag{2}$$

where R is the line equivalent resistance; ω_1 is the angular line-frequency; L is the equivalent inductance which includes the inverter-side inductance L_1 and the grid-side inductance L_2. The other variables are transformed from the variables denoted in Fig. 2.

As shown in (1), there are strong couplings between the *d*-axis and *q*-axis. With the commonly-used dual closed-loop control strategy based on the feedforward decoupling and the PI controller, the inner current loop and the outer dc-link voltage loop can be given by

$$\begin{cases} v_d = (K_p + \dfrac{K_i}{s})(i_d^* - i_d) - \omega_1 L i_q + e_d \\ v_q = (K_p + \dfrac{K_i}{s})(i_q^* - i_q) + \omega_1 L i_d + e_q \end{cases}, \tag{3}$$

$$i_d^* = (K_{vp} + \frac{K_{vi}}{s})(u_{dc}^* - u_{dc}) \tag{4}$$

where K_p, K_i, K_{vp}, and K_{vi} are the proportional and integral gain of the current loop and the dc-link voltage loop, respectively; i_d^* and i_q^* are the reference current of *d*-axis and *q*-axis; u_{dc}^* is the dc-link reference voltage. With the grid voltage feedforward term (e_d and e_q), the dynamic response of the system is enhanced [24], and theoretically, the current harmonics caused by the distorted grid voltage can be totally eliminated through the feedforward voltage compensation. However, in digital control systems, i_d, i_q, e_d, e_q, and u_{dc} are not the real values but the measured (sampled) values from the power circuit; v_d and v_q are not the output voltages of the inverter but the reference voltages given to the PWM. There are errors between these variables and their real values. Taking these errors into account, (3) and (4) should be expressed as

$$\begin{cases} v_d^* = (K_p + \dfrac{K_i}{s})(i_d^* - i_{dM}) - \omega_1 L i_{qM} + e_{dM} \\ v_q^* = (K_p + \dfrac{K_i}{s})(i_q^* - i_{qM}) + \omega_1 L i_{dM} + e_{qM} \end{cases}, \tag{5}$$

$$i_d^* = (K_{vp} + \frac{K_{vi}}{s})(u_{dc}^* - u_{dcM}) \tag{6}$$

where i_{dM}, i_{qM}, e_{dM}, e_{qM}, and u_{dcM} are the measured values; v_d^* and v_q^* are the reference voltage given to the PWM. The expressions between the real values and the measured values can be given by

$$\begin{cases} \begin{bmatrix} i_d \\ i_q \end{bmatrix} = \begin{bmatrix} i_{dM} \\ i_{qM} \end{bmatrix} + \begin{bmatrix} i_{dE} \\ i_{qE} \end{bmatrix} \\ \begin{bmatrix} e_d \\ e_q \end{bmatrix} = \begin{bmatrix} e_{dM} \\ e_{qM} \end{bmatrix} + \begin{bmatrix} e_{dE} \\ e_{qE} \end{bmatrix} \\ \begin{bmatrix} v_d \\ v_q \end{bmatrix} = \begin{bmatrix} v_d^* \\ v_q^* \end{bmatrix} + \begin{bmatrix} v_{dE} \\ v_{qE} \end{bmatrix} \\ u_{dc} = u_{dcM} + u_{dcE} \end{cases} \tag{7}$$

where i_{dE}, i_{qE}, e_{dE}, e_{qE}, and u_{dcE} are the measurement errors; v_{dE} and v_{qE} are the output voltage errors. With these errors taken into account, the feedforward decoupling method can be illustrated in Fig. 3.

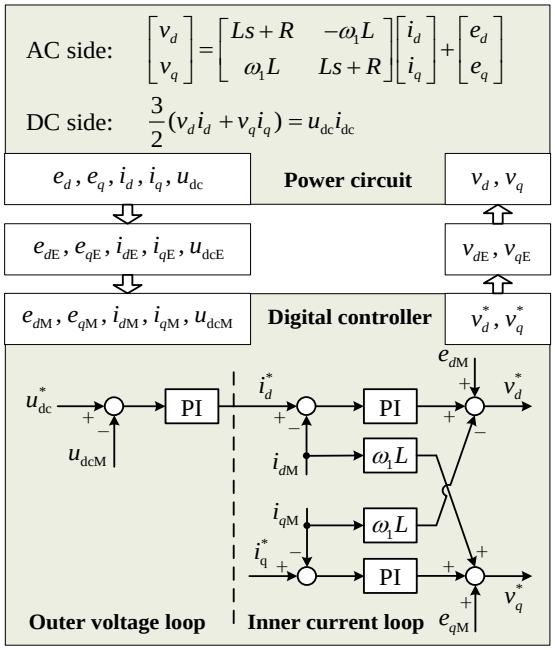

Fig. 3. Feedforward decoupling method with the errors taken into account.

With (1), (5), and (7), the output currents of the inverter can be derived as

$$\begin{bmatrix} i_d \\ i_q \end{bmatrix} = \frac{1}{Ls+R+K_p+\dfrac{K_i}{s}} \begin{bmatrix} K_p+\dfrac{K_i}{s} & \omega_1 L & -1 \\ K_p+\dfrac{K_i}{s} & -\omega_1 L & -1 \end{bmatrix} \cdot \begin{bmatrix} i_q^* + i_{qE} & i_d^* + i_{dE} \\ i_{dE} & i_{qE} \\ e_{qE} - v_{qE} & e_{dE} - v_{dE} \end{bmatrix}. \tag{8}$$

As seen in (8), the errors between the digital controller and the power circuit have a negative impact on the output currents of the inverter. And the terms $e_{dE} - v_{dE}$ and $e_{qE} - v_{qE}$ will determine the grid voltage feedforward precision. The detailed discussion about the errors in the grid voltage feedforward loop concerned in this paper is given as follows.

The ac voltage measurement errors e_{dE} and e_{qE} mainly come from sensors, signal conditioning circuits and A/D chips. With the fast response and high precision of Hall sensors [34], and the fast throughput 16-bit A/D chip AD7656 adopted in this paper, the errors caused by the Hall sensors and A/D chips can be ignored. However, the conditioning circuits may distort the measured signals and need to be carefully designed.

One of the factors leading to the output voltage errors v_{dE} and v_{qE} is the ZOH characteristic of PWM [35], [36]. The transfer function of PWM in the frequency (s) domain can be expressed as

$$G_{\mathrm{PWM}}(s) = K_{\mathrm{PWM}} \frac{1 - e^{-T_{\mathrm{PWM}} s}}{s} \tag{9}$$

where K_{PWM} and T_{PWM} are the gain and period of PWM, respectively. It is complicated to discretize (9) in z domain when the control period T_c of the controller and the period of PWM are the same [23], [35]. Ideally, the discrete form of (9) should be $z^{-0.5}$ (discrete time T_c=T_{PWM}) since the fundamental component of the inverter output voltage is delayed by $T_{\mathrm{PWM}}/2$ due to the ZOH characteristic [35], [36]. However, the discrete term $z^{-0.5}$ can't be realized by the digital controller due to the minimum unit of discretization is based on the control period of the digital controller. In this paper, a control frequency of 10kHz and a switching frequency of 5kHz (T_{PWM} doubles T_c) are adopted, so that the PWM term can be discretized as z^{-1} (discrete time T_c= $T_{\mathrm{PWM}}/2$). And with higher control frequency, better control accuracy and dynamic performance can also be achieved [37]. Besides the aforementioned ZOH characteristic of PWM, several other elements, e.g. the dead-time of PWM, the device turn-on and turn-off delays, and the device voltage drop can also cause the output voltage errors [38]. This portion of errors can be minimized by the dead-time compensation to some extent and will not be considered in this paper.

In addition, in a digital control system, the reference voltage given to the PWM must be calculated before the PWM update. Therefore, one control period delay in the digital controller before the PWM update is indispensable from the control perspective [23].

In summary, the ac-voltage measurement errors (e_{dE} and e_{qE}) due to the conditioning circuit, the output voltage errors (v_{dE} and v_{qE}) due to the ZOH characteristic of PWM, and the control delay of the digital controller for PWM update (digital control) together decide the grid voltage feedforward precision which can directly affect the performance of the grid voltage feedforward control. And how these errors affect the performance of the conventional grid voltage feedforward strategy is analyzed in detail as follows.

III. Impact of the Errors in Feedforward Loop on the Grid Voltage Feedforward Strategy

In order to simplify the analysis how the errors in the feedforward loop affect the grid voltage feedforward strategy, premises are assumed as follows: 1) Only a single harmonic exists in the grid voltage; 2) The grid is in stable operation, i.e. no transient conditions are taken into account.

Given the fundamental frequency is ω_1, the h^{th} order grid voltage harmonic can be expressed as

$$e_h(t) = E_h \cos(h\omega_1 t + \varphi_h) \tag{10}$$

where E_h, $h\omega_1$, and φ_h are the amplitude, angle frequency, and phase angle of the h^{th} order grid voltage harmonic.

Assume the feedforward term lags the real grid voltage by t_d (t_d<0). Correspondingly, the phase delay φ_{dh} of the h^{th} order grid voltage harmonic can be expressed as φ_{dh}=$h\omega_1 t_d$, φ_{dh}<0. It should be noted that t_d is not related to h, but φ_{dh} is. And the amplitude error is $\varepsilon_h E_h$ (-1<ε_h<1). With the errors in the grid voltage feedforward loop, the feedforward grid voltage can be expressed as

$$v_h(t) = (1+\varepsilon_h) E_h \cos(h\omega_1 t + \varphi_h + \varphi_{dh}) . \tag{11}$$

With the grid voltage feedforward compensation, the remnant voltage harmonic can be derived from (10) and (11) as

$$\begin{aligned} v_{rh}(t) &= e_h(t) - v_h(t) \\ &= E_h \sqrt{1 + (1+\varepsilon_h)^2 - 2(1+\varepsilon_h)\cos\varphi_{dh}}\, \cos(h\omega_1 t + \varphi_h + \delta_h) \end{aligned} \tag{12}$$

where $\delta_h = \begin{cases} \tan^{-1} \dfrac{-(1+\varepsilon_h)\sin\varphi_{dh}}{1-(1+\varepsilon_h)\cos\varphi_{dh}}, & 1-(1+\varepsilon_h)\cos\varphi_{dh} > 0 \\ \tan^{-1} \dfrac{-(1+\varepsilon_h)\sin\varphi_{dh}}{1-(1+\varepsilon_h)\cos\varphi_{dh}} + \pi, & 1-(1+\varepsilon_h)\cos\varphi_{dh} < 0 \end{cases}$.

Define the amplitude ratio of the remnant voltage harmonic to the original grid voltage harmonic as the grid voltage harmonic residual rate η, which can be given by (13) derived from (12).

$$\eta = \sqrt{1 + (1+\varepsilon_h)^2 - 2(1+\varepsilon_h)\cos\varphi_{dh}} \times 100\% . \tag{13}$$

Here, the amplitude error and phase delay are analyzed separately:

1) When φ_{dh}=0, (13) can be transformed to

$$\eta = \sqrt{1 + (1+\varepsilon_h)^2 - 2(1+\varepsilon_h)} \times 100\% = \varepsilon_h \times 100\% . \tag{14}$$

As seen in (14), when there is no phase delay, η is equal to ε_h. Among the errors in the grid voltage feedforward loop, the control delay of the digital controller and the ZOH characteristic of PWM won't affect amplitude of the harmonics. And with the maximally flat magnitude response of the conditioning circuit designed latter in Section V, the low order harmonics will approximately have the same the amplitude errors ε_h. Hence, the amplitude errors can be minimized by adjusting the gains of the sampled signals in software within an acceptable range.

2) When ε_h=0, (13) can be transformed to

$$\eta = \sqrt{2 - 2\cos\varphi_{dh}} \times 100\% = \sqrt{2 - 2\cos(h\omega_1 t_d)} \times 100\% . \tag{15}$$

As seen in (15), when there is no amplitude errors, η is the function of h and t_d. The relation among η, h, and t_d given in (15) can be illustrated in Fig. 4(a) where only curves with h=1, 3, 5, 7 are plotted to make the figure clear. As seen, for the h^{th} order harmonic, when φ_{dh} is even times of π, η becomes zero; when φ_{dh} is odd times of π, η values the maximum 200%. It is indicated that if phase delays exist in the grid voltage feedforward loop, the feedforward term can even intensify the impact of grid voltage harmonics on the system. In practice, the

delay time in the grid voltage feedforward loop is smaller than 500μs, and the relation among η, h, and t_d is illustrated in Fig. 4(b). As seen, if t_d equals zero, the conventional grid voltage feedforward control can totally cancel the grid voltage harmonics to eliminate its impact on the system. However, the errors caused by the conditioning circuit, the digital control, and PWM lead to the delay in the grid voltage feedforward loop, e.g. in the high-power inverters with a low switching frequency of 2kHz, the delay can be more than 250μs. Consequently, the performance of the conventional grid voltage feedforward control is greatly degraded. In this paper, an open-loop simplified repetitive predictor is proposed to compensate the delay in the grid voltage feedforward loop, and the performance of the grid voltage feedforward strategy is effectively improved.

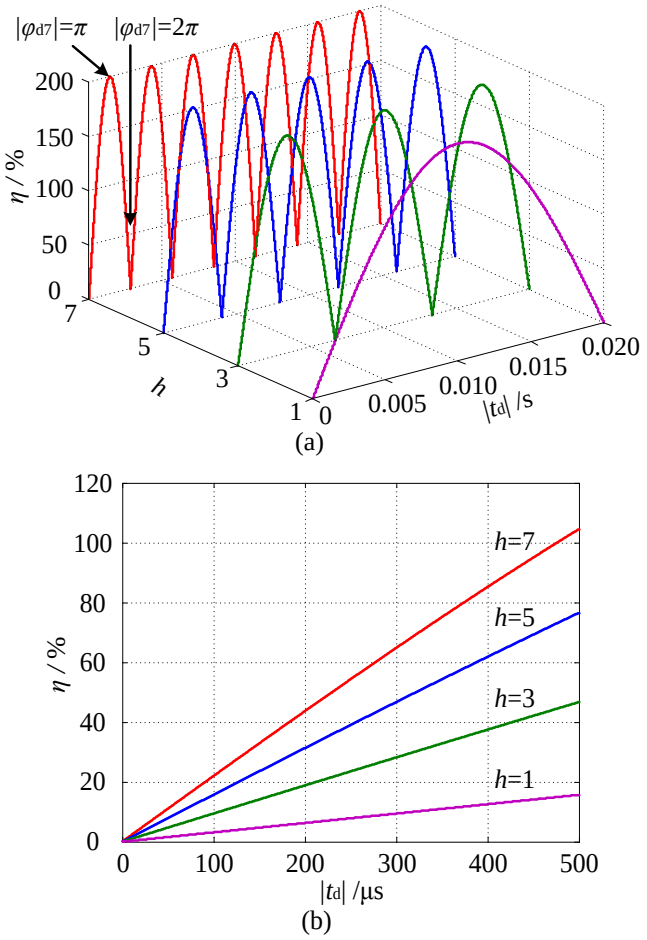

Fig. 4. The variation of η with h and t_d (h =1, 3, 5, 7): (a) $|t_d|$ form 0s to 0.02s, (b) $|t_d|$ form 0s to 500μs.

IV. Open-Loop Simplified Repetitive Predictor and Its Hysteresis Error Analysis

As the fundamental and harmonic components of grid voltage are repetitive every cycle when the grid is stable, it is very suitable to use the repetitive predictor to predict the grid voltage feedforward term several steps ahead, which can compensate the delays and enhance the precision of the grid voltage feedforward [25]-[27]. In this section, based on the conventional closed-loop repetitive predictor [25], an open-loop simplified repetitive predictor is proposed with unchanged steady-state and dynamic performance. The computational and design complexity is reduced and there is no stability issue with the simplified predictor. The hysteresis error is analyzed accounting for the grid voltage dip.

A. A Simple Hysteresis Repetitive Predictor

Take each control period T_c as a step, and in a fundamental cycle there are N steps in total. Due to the periodic grid voltage, the sampled grid voltage of the former cycle can be taken as the predicted values of the current cycle, which makes it possible to predict the grid voltage feedforward term for any p ($0 \leqslant p \leqslant N$) steps ahead. This method can be taken as a simple hysteresis repetitive predictor illustrated in Fig. 5, where $y(k)$ is the current value; $y(k+p-N)$ is the past sampled value with $N-p$ steps hysteresis; $\hat{y}(k+p)$ is the predictive value ahead p steps. In a digital control system, it is easy to store the sampled grid voltage of the former cycle, which makes it possible to implement this simple hysteresis repetitive predictor.

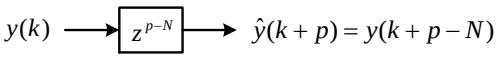

Fig. 5. Simple hysteresis repetitive predictor.

Fig. 6 shows the performance of the simple hysteresis repetitive predictor in an extreme situation, using a sine wave with an abrupt change to zero at 0.06s. In the steady state, the input signal is predicted by p steps ahead as expected; However in the dynamic state, the N-p steps hysteresis error appears. The phenomenon is due to the fact that the simple hysteresis repetitive predictor takes the N-p steps hysteresis as an equivalent prediction with p steps ahead. If the simple hysteresis repetitive predictor is used to predict the grid voltage feedforward term by p steps ahead, it may lead to over currents of the system and potential devices failure when the grid voltage dip occurs. The simple hysteresis repetitive predictor is not directly applicable as the capability of low voltage ride through (LVRT) is generally required in a renewable power system [39].

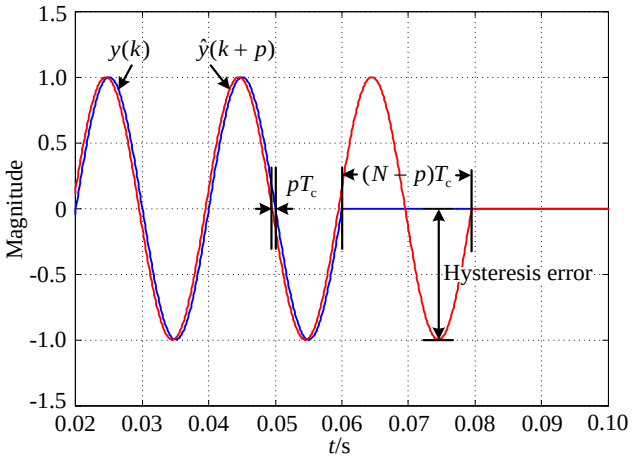

Fig. 6. Performance of the simple hysteresis repetitive predictor (p=5 and N=200).

B. Conventional Closed-Loop Repetitive Predictor

The typical scheme of the closed-loop repetitive predictor comprises a repetitive controller, a compensator, and a proportional term, as shown in Fig. 7. When the predicted signal is periodic every cycle, the error between the current value and the predictive value also appears as a fixed periodic waveform. The closed-loop repetitive predictor adds the repetitive error

extracted by the repetitive controller to the current value through a closed-loop feedback path to obtain the predictive value. Each part of the closed-loop repetitive predictor is discussed as follows:

(1) **Repetitive controller**. As shown in Fig. 7, $Q(z)z^{-N}$ is the internal model of the repetitive controller. With $Q(z)$=1, like the general integral achieving a zero steady-state error for harmonics [6], the repetitive controller has an infinite gain and zero phase shift at the fundamental frequency and its multiple frequencies [13], [14]. However, the poles of the open-loop transfer function which exist on unit circle may lead to instability [27]. In practice, considering both control accuracy and stability, $Q(z)$ is selected as less but close to one to make the repetitive controller behave like an integrator.

(2) **Compensator**. The compensator z^{p} makes it possible to predict the signal ahead p steps. And to be implemented in a digital controller, the hysteresis term z^{-N} must be added.

(3) **Proportional term**. The proportional term k_r determines the influence of the compensation term $y_c(k+p-N)$ on the closed-loop repetitive predictor to keep a balance between stability and convergence speed [25].

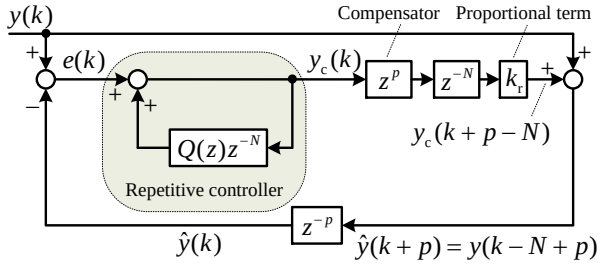

Fig. 7. Conventional closed-loop repetitive predictor.

In Fig. 7, $\hat{y}(k)$ is the prediction of current value, $\hat{y}(k)=\hat{y}(k+p)z^{-p}$; $e(k)$ is the predictive error between $y(k)$ and $\hat{y}(k)$; $y_c(k)$ is the integral of $e(k)$ by the repetitive controller. With $y_c(k)$ ahead p steps (the z^{p} term), delayed by N steps (the z^{-N} term), and then multiplied by k_r, the compensation term $y_c(k+p-N)$ can be calculated. By adding this compensation term to the current value, $y(k+p-N)$ is obtained which can be taken as the predictive value $\hat{y}(k+p)$ during the steady state.

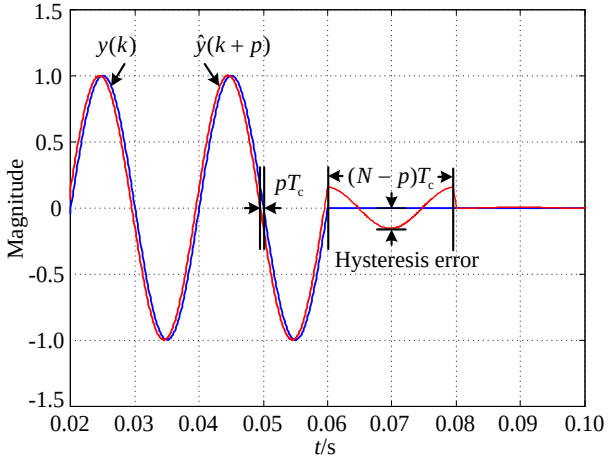

Fig. 8. Performance of the closed-loop repetitive predictor (p=5, N=200, $Q(z)$=0.95, and k_r=0.98).

The repetitive predictor obtains the predictive value by adding the compensation term certain steps ahead to the current value. It has better dynamic performance compared to the simple hysteresis repetitive predictor which obtains the predictive value directly from the former cycle. Fig. 8 shows the performance of the closed-loop repetitive predictor in an extreme situation. As seen, in the steady state, the input signal is predicted by p steps ahead; and in the dynamic state, the N-p steps hysteresis error appears as the simple hysteresis repetitive predictor. In contrast to the hysteresis error of the simple hysteresis repetitive predictor shown in Fig. 6, this hysteresis error have been effectively reduced, whose maximum value is related to $Q(z)$ and k_r.

C. Open-Loop Simplified Repetitive Predictor

Although the above mentioned closed-loop repetitive predictor can predict the periodic signals p steps ahead and decrease the hysteresis error, the closed-loop structure and several terms existing in the predictor make the control scheme complicated. Further, the stability of the control loop need to be carefully considered. To overcome these issues, an open-loop simplified repetitive predictor is proposed.

The transfer function of the closed-loop repetitive predictor shown in Fig. 7 can be expressed as

$$G_{CR}(z)=\frac{\hat{y}(k+p)}{y(k)}=\frac{1-Q(z)z^{-N}+k_r z^{p-N}}{1-Q(z)z^{-N}+k_r z^{-N}}. \tag{16}$$

Let $Q(z)$=1 and k_r=1, (16) can be simplified as

$$G_{OR}(z)=\frac{\hat{y}(k+p)}{y(k)}=1-z^{-N}+z^{p-N}. \tag{17}$$

The predictor shown in (17) can be taken as an open-loop simplified repetitive predictor which has a clear physical meaning. For better comprehension, the open-loop simplified repetitive predictor shown in Fig. 9 is analyzed from the viewpoint of steady-state and dynamic performances, respectively.

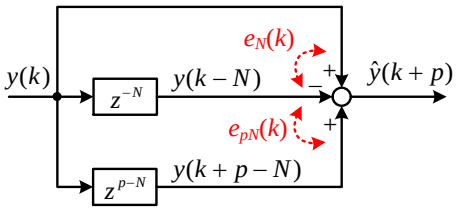

Fig. 9. Open-loop simplified repetitive predictor.

From the viewpoint of steady-state performance, the error $e_N(k)$ between $y(k)$ and $y(k-N)$ is zero due to the waveform of the periodic signal is repetitive every cycle. In this situation, the open-loop simplified repetitive predictor takes the N-p steps hysteresis signal as the prediction p steps ahead, like the simple hysteresis repetitive predictor shown in Fig. 5.

From the viewpoint of dynamic performance, the error $e_{pN}(k)$ between $y(k-N)$ and $y(k+p-N)$, which plays the same role as the compensation term $y_c(k+p-N)$ in the closed-loop repetitive predictor, is added to the current value to obtain the predictive value. Good dynamic performances of the open-loop simplified repetitive predictor and the closed-loop repetitive predictor are based on that they both obtain the predictive value by adding the compensation term ahead certain steps to the current value.

Compared to the performance of the closed-loop repetitive predictor shown in Fig. 8, similar steady-state and dynamic performance of the open-loop simplified repetitive predictor given in (17) is shown in Fig. 10 with the maximum hysteresis error exactly valued 15.68% (p=5). Due to the elimination of the repetitive controller and proportional term of the closed-loop predictor, the computational complexity of the open-loop simplified repetitive predictor is reduced. Further, given its open-loop structure without any integrator or differentiator, the instability problem does not exist.

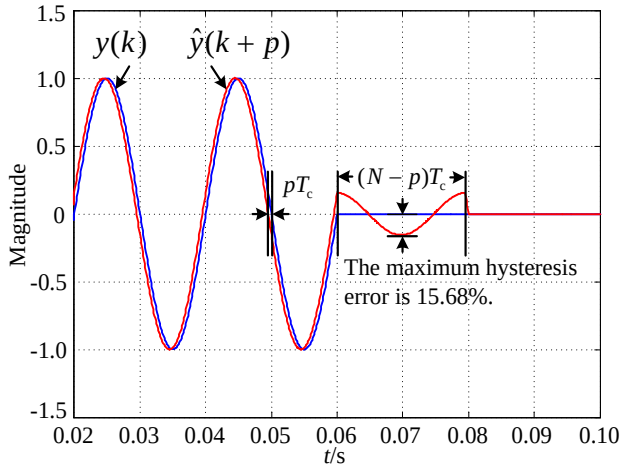

Fig. 10. Performance of the open-loop simplified repetitive predictor (p=5 and N=200).

In addition, without the limitation of the parameters ($Q(z)$ and k_r) for stability consideration, the precision of the open-loop simplified repetitive predictor is better than that of the conventional closed-loop repetitive predictor. The small difference between the output of the conventional predictor ($Q(z)$=0.95, k_r=0.98) and the simplified predictor is shown in Fig. 11. As seen, the difference between the two predictors is less than 0.008 at both steady and dynamic states. When $Q(z)$=1 and k_r=1, the difference will become zero.

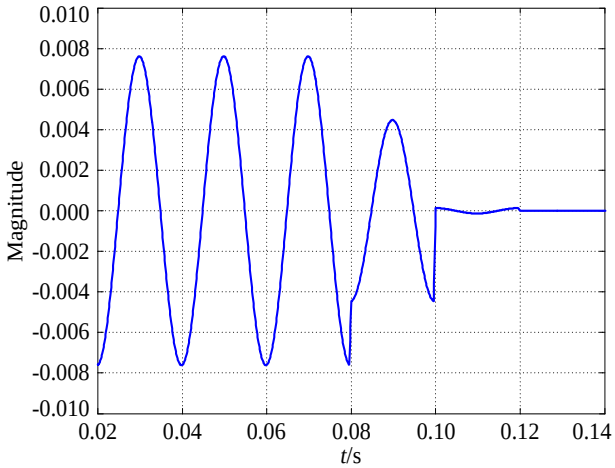

Fig. 11. Difference between the output of the conventional repetitive predictor ($Q(z)$=0.95, k_r=0.98) and the simplified repetitive predictor.

D. Analysis on Hysteresis Error of the Open-Loop Simplified Repetitive Predictor

In practice, when the grid voltage dip occurs, only the fundamental grid voltage is concerned. Hence, assuming a fundamental sinusoidal signal $y(k)$, with the open-loop simplified repetitive predictor, the differential equation in the steady state can be expressed as

$$\hat{y}(k+p) = y(k) - y(k-N) + y(k-N+p) = y(k) + e_{pN}(k) \quad (18)$$

Assuming that the signal changes from $y(k)$ to $\zeta y(k)$ ($0<\zeta<1$), the differential equation in the hysteresis N-p steps can be given by

$$\zeta \hat{y}(k+p)_{N-p} = \zeta y(k) + e_{pN}(k) . \quad (19)$$

With the input signal $\zeta y(k)$, the differential equation in the steady state is

$$\zeta \hat{y}(k+p) = \zeta y(k) + \zeta e_{pN}(k) . \quad (20)$$

With (19) and (20), the hysteresis error $e_\zeta(k)$ of the open-loop simplified repetitive predictor can be derived as

$$e_\zeta(k) = \zeta \hat{y}(k+p)_{N-p} - \zeta \hat{y}(k+p) = e_{pN}(k)(1-\zeta) . \quad (21)$$

As is seen in (21), $e_\zeta(k)$ is directly proportional to $e_{pN}(k)$, and inversely proportional to ζ. Adopt the conclusion in (15) to (21), the maximum hysteresis error e_ζ can be derived as

$$e_\zeta = (1-\zeta)\sqrt{2-2\cos(\omega_1 p T_c)} \times 100\% . \quad (22)$$

According to (22), e_ζ is plotted in Fig. 12 with ζ and p varying. With the development of the digital control system, the delay in the whole grid voltage feedforward loop is usually within 500μs, which makes p a small integer. Thereupon, even with a sudden dip in grid voltage (ζ is small), e_ζ will be small and acceptable. For example, when p=3, the maximum hysteresis error will be always within 10%. This means the open-loop simplified repetitive predictor will hardly affect the LVRT performance.

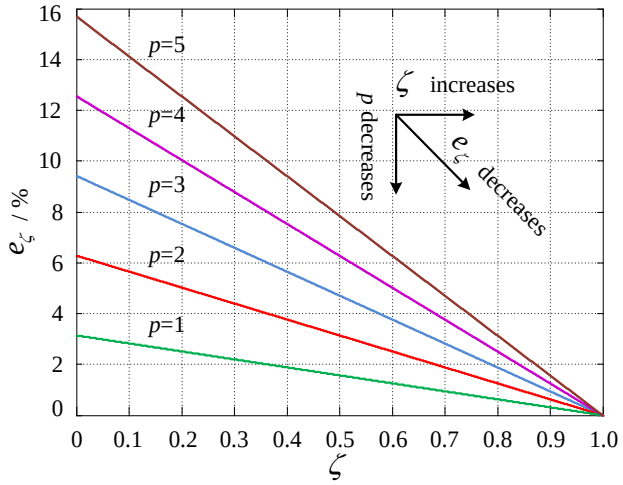

Fig. 12. e_ζ with ζ and p varying.

V. Design of the Signal Conditioning Circuit

The conditioning circuits play an important role on the sampling path, and special attention should be paid to its design. A typical conditioning circuit with the commonly used 2nd order Butterworth low-pass filter [28], [29] is shown in Fig. 13. The output signal from the sensor in a current form is converted into the voltage signal by the precision sampling resistor r_s. Through the voltage follower, the signal is buffered with the enhanced driving capability. Then by the 2nd order Butterworth low-pass filter, the high-frequency interference in the signal is eliminated,

and the signal is adjusted to satisfy the input range of the A/D chips. Lastly, the maximum amplitude of the signal is constrained by the clamping circuit. In this section, the 2nd order Butterworth low-pass filter which may cause the signal distortion is designed with the maximally flat magnitude response and the almost linear phase response. In addition, the relation between the delay time and the cutoff angular frequency of the 2nd order Butterworth low-pass filter is analyzed.

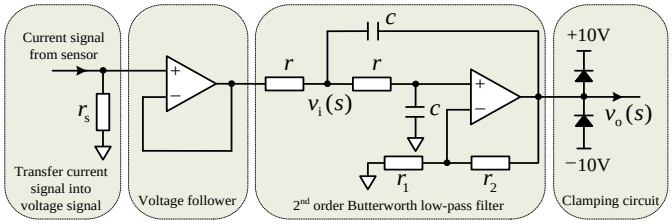

Fig. 13. A typical conditioning circuit.

A. Design of the Second Order Butterworth Low-Pass Filter

The transfer function of the 2nd order Butterworth low-pass filter shown in Fig. 13 can be expressed as [28]

$$G_B(s)=\frac{v_o(s)}{v_i(s)}=\frac{G_{Bp}}{1+(3-G_{Bp})rcs+(rcs)^2} \tag{23}$$

where, G_{Bp} is the gain of the filter, $G_{Bp}=1+r_2/r_1$. Only if $G_{Bp}<3$, the circuit will be stable, i.e. the coefficient of s in the denominator of (23) should be greater than zero. ω_c is the cutoff angular frequency, $\omega_c=1/rc$. Define the quality factor $Q=1/(3-G_{Bp})$, and its physical meaning is the ratio of $|G_B(s)|$ to G_{Bp} when $\omega=\omega_c$. Substituting the operator s with $j\omega$, (23) can be transformed to

$$G_B(\omega)=\frac{G_{Bp}}{1-(\frac{\omega}{\omega_c})^2+j\frac{1}{Q}\cdot\frac{\omega}{\omega_c}}. \tag{24}$$

With (24), the expression of the amplitude- and phase-frequency responses of the 2nd order Butterworth low-pass filter can be respectively expressed as

$$|G_B(\omega)|=\frac{G_{Bp}}{\sqrt{\left[1-(\frac{\omega}{\omega_c})^2\right]^2+\left[\frac{1}{Q}\cdot\frac{\omega}{\omega_c}\right]^2}}, \tag{25}$$

$$\angle G_B(\omega)=-\arctan\frac{\frac{\omega}{\omega_c}}{Q[1-(\frac{\omega}{\omega_c})^2]}. \tag{26}$$

The maximally flat magnitude response of the 2nd order Butterworth low-pass filter with $Q=0.707$ has been indicated in many literatures [28], [29], only a simple explanation is given here. Substitute $Q=0.707$ into (25), the amplitude response is transformed to

$$|G_B(\omega)|=\frac{G_{Bp}}{\sqrt{1+(\frac{\omega}{\omega_c})^4}}. \tag{27}$$

When $\omega/\omega_c<<1$, $(\omega/\omega_c)^4\approx 0$. $|G_B(s)|$ approximately equals to the constant G_{Bp}, which can be taken as a simple illustration to verify the maximally flat amplitude response of the 2nd order Butterworth low-pass filter.

The phase response curves expressed by (26) will cross the two points (0, 0) and (ω_c, $-\pi/2$) as seen in Fig. 14. By joining the two points with a straight line, the expression of the standard linear phase response can be expressed as

$$\angle G_B(\omega)^*=\frac{-\pi}{2}\cdot\frac{\omega}{\omega_c}. \tag{28}$$

As Q varies, the best-fit phase response curve of the standard linear phase response is verified by the least squares method [40]. In the interval $\omega/\omega_c\in[0, 1]$, define the fit degree M as

$$M=\sum\left(\angle G_B(\omega)-\angle G_B(\omega)^*\right)^2$$
$$=\sum_{\frac{\omega}{\omega_c}=0,\,0.001,\,0.002\cdots}^{\frac{\omega}{\omega_c}=1}\left(-\arctan\frac{\frac{\omega}{\omega_c}}{Q[1-(\frac{\omega}{\omega_c})^2]}+\frac{\pi}{2}\cdot\frac{\omega}{\omega_c}\right)^2. \tag{29}$$

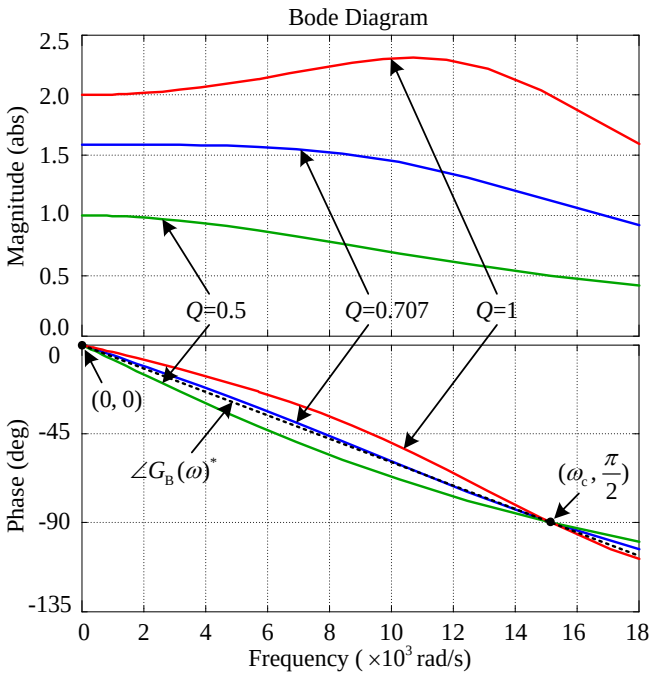

Fig. 14. Frequency responses of second order Butterworth low-pass filter with different Q (Q=0.5, 0.707, 1).

Fig. 15 shows the variation of M with Q. As seen, when $Q=0.671$, M is minimum, i.e. the phase response $\angle G_B(\omega)$ fits the standard linear-phase-response curve $\angle G_B(\omega)^*$ the best. Although Q valued 0.707 is not the best choice for the linear phase response, taking both the magnitude and phase response into account, Q is selected as 0.707 at last. As illustrated in Fig. 14, compared to the responses with other Q values, the 2nd order Butterworth low-pass filter with $Q=0.707$ has the maximally flat magnitude response and the almost linear phase response below the cutoff angular frequency.

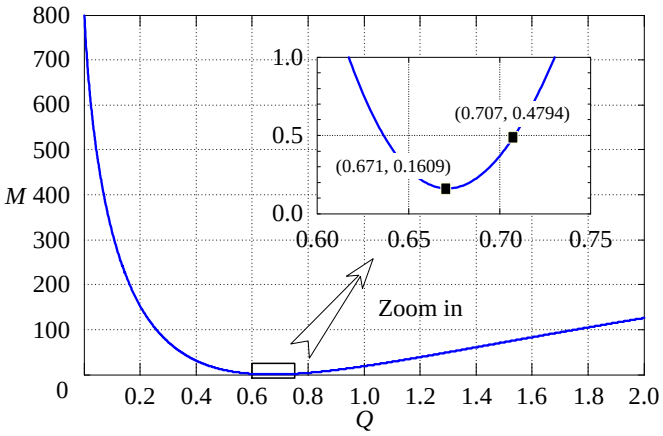

Fig. 15. *M*-*Q* curve.

B. Relation between the Delay Time and the Cutoff Angular Frequency of the Second Order Butterworth Low-Pass Filter

With the almost linear phase response of the 2nd order Butterworth low-pass filter, the delay phase of the h^{th} harmonic can be approximatively expressed as

$$\angle G_{Bh}(\omega) = \frac{-\pi}{2} \cdot \frac{\omega_h}{\omega_c}. \tag{30}$$

The proportional expression between the delay time and phase is given by

$$\frac{t_{Bd}}{T_h} = \frac{\angle G_{Bh}(\omega)}{2\pi} \tag{31}$$

where t_{Bd} is the delayed time; T_h is the period of the h^{th} harmonic. With (30) and (31), the expression of the delay time and the cutoff angular frequency can be derived as

$$t_{Bd} = \frac{-\pi}{2\omega_c} \tag{32}$$

where the negative sign donates it is a delay time.

According to the analysis above, t_{Bd} is selected as 103μs, about one control period T_c (T_c=100μs), for ω_c=15151.3rad/s (2411.4Hz), Q=0.707, r=3kΩ, and c=22nF. Selecting the delay time t_{Bd} as several times of T_c is out of the consideration that the open-loop simplified repetitive predictor adopted in this paper can only predict the feedforward term certain steps ahead, i.e. the delay time t_{Bd} can be exactly compensated by the predictor.

VI. Current Control Loop Design and Delay-Compensation State of the Grid Voltage Feedforward Loop

A. Design of the Current Loop

Considering the aforementioned errors, taking the *d*-axis current control loop for example, the current control loop based on the improved grid voltage feedforward strategy is shown in Fig. 16, where each term is denoted in Table I. The terms in Table I are discretized by the bilinear transform (also known as Tustin's method, $s=\frac{2}{T_c}\cdot\frac{z-1}{z+1}$) which is commonly used in engineering applications [41].

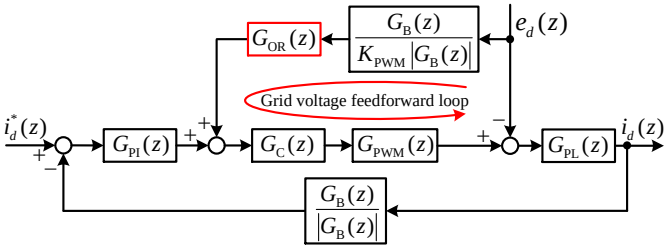

Fig. 16. *d*-axis current control loop based on the improved grid voltage feedforward strategy.

TABLE I
Discretization of the Terms in the Current Control Loop

Symbol	Term	*s* domain	*z* domain
$G_{PI}(z)$	PI controller	$K_p + \frac{K_i}{s}$	$\frac{K_iT_c + 2K_p + (K_iT_c - 2K_p)z^{-1}}{2 - 2z^{-1}}$
$G_C(z)$	Control delay	—	z^{-1}
$G_{PWM}(z)$	ZOH characteristic of PWM	$K_{PWM}\frac{1-e^{-T_{PWM}s}}{s}$	$K_{PWM}z^{-1},\ (T_c = T_{PWM}/2)$
$G_{PL}(z)$	Plant	$\frac{1}{sL+R}$	$\frac{T_c + T_cz^{-1}}{RT_c + 2L + (RT_c - 2L)z^{-1}}$
$G_{OR}(z)$	Open-loop simplified repetitive predictor	—	$z^p \Leftrightarrow 1 - z^{-N} + z^{p-N}$
$G_B(z)$	2nd order Butterworth low-pass filter	$\frac{G_{Bp}}{1+(3-G_{Bp})rcs+(rcs)^2}$	$\frac{G_{Bp}T_c^2(1+2z^{-1}+z^{-2})}{T_c^2+2(3-G_{Bp})rcT_c+4r^2c^2+(2T_c^2-8r^2c^2)z^{-1}+[T_c^2-2(3-G_{Bp})rcT_c+4r^2c^2]z^{-2}}$

Note that with T_c=T_{PWM}/2 as mentioned in Section II, the PWM term is discretized as z^{-1}. And to simplify the analysis, $G_{OR}(z)$ in (17) is simplified as an equivalence z^p in steady state.

The closed-loop transfer function of the current loop shown in Fig. 16 can be given by

$$H_d(z)=\frac{i_d(z)}{i_d^*(z)}=\frac{G_{\mathrm{PI}}(z)G_{\mathrm{C}}(z)G_{\mathrm{PWM}}(z)G_{\mathrm{PL}}(z)}{1+\dfrac{G_{\mathrm{B}}(z)}{|G_{\mathrm{B}}(z)|}G_{\mathrm{PI}}(z)G_{\mathrm{C}}(z)G_{\mathrm{PWM}}(z)G_{\mathrm{PL}}(z)}. \quad (33)$$

And the admittance of output current to grid voltage can be derived as

$$Y(z)=\frac{i_d(z)}{e_d(z)}=\frac{G_{\mathrm{PL}}(z)\left[\dfrac{G_{\mathrm{B}}(z)}{K_{\mathrm{PWM}}|G_{\mathrm{B}}(z)|}G_{\mathrm{OR}}(z)G_{\mathrm{C}}(z)G_{\mathrm{PWM}}(z)-1\right]}{1+\dfrac{G_{\mathrm{B}}(z)}{|G_{\mathrm{B}}(z)|}G_{\mathrm{PI}}(z)G_{\mathrm{C}}(z)G_{\mathrm{PWM}}(z)G_{\mathrm{PL}}(z)}. \quad (34)$$

Comparing (33) with (34), they have the same closed-loop poles which can indicate whether the system is stable or not. Hence, as long as one of the two transfer functions is stable, the stability of the entire current loop is guaranteed. Regarding the PI controller in (33), controller gains can be selected as $K_p/K_i=L/R$ to achieve the pole-zero cancellation [42]. The cancelled pole and zero on the root locus of the current loop are shown in Fig. 17(a) for L=0.4mH, R=0.01Ω. As also seen, when K_p<2.16, the closed-loop characteristic roots are within the unit circle, which indicates a stable current loop [43]. K_p is selected as 0.681 on the root locus to achieve the optimal damping ratio ξ of 0.707 decided by the dominant poles. Correspondingly, K_i =17 and the cutoff frequency of the current loop is 270Hz. With the selected K_p and K_i, the gain margin (GM) and the phase margin (PM) of the current loop are 16.4dB and 67.2°, respectively, which further indicates the current loop is stable [44]. And the step response of the current loop is shown in Fig. 17(b) with desired specifications. Regarding the loop from e_d to i_d, with the errors in the grid voltage feedforward loop is compensated by the simplified repetitive predictor, the grid voltage, which is usually taken as a perturbation, is well cancelled, making it have little influence on the output current i_d. In addition, the dc-link voltage loop is designed with a classic method according to [33]. Considering both dynamic response and stability, the parameters of the PI controller in dc-link voltage loop are selected as K_{vp}=10 and K_{vi}=800 with GM=29.8dB and PM=63.5°.

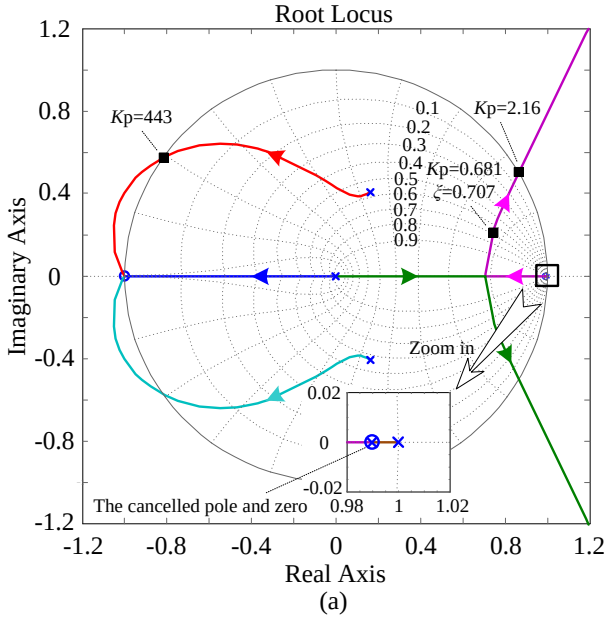

(a)

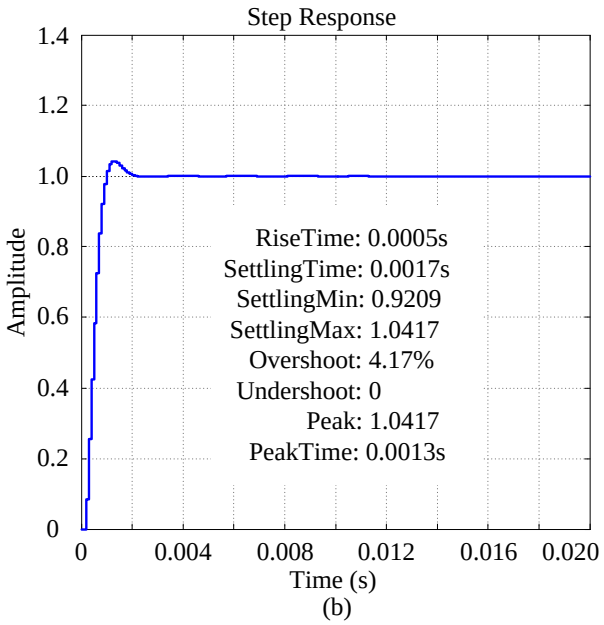

(b)

Fig. 17. Design of current loop: (a) root locus of the current loop with K_p varying from 0 to infinite (b) step response of the current loop with K_p=0.681.

B. Analysis of the Delay-Compensation State in the Grid Voltage Feedforward Loop

As seen in the numerator of (34), if $G_{OR}(z)$ can totally compensate the delays in $G_B(z)$, $G_C(z)$ and $G_{PWM}(z)$, the admittance of output current to grid voltage will be zero in the whole frequency range, i.e. all the harmonic admittances are zero so that the improved grid voltage feedforward strategy can effectively minimize the current harmonics caused by the distorted grid voltage. The admittance-frequency curves with p varying from 0 to 5 are shown in Fig. 18, where p is the number of steps predicted by the predictor. Due to the non-ideal frequency response of the 2nd order Butterworth low-pass filter, the admittance-frequency curves are not regular. However, in the low frequency range (below 1870Hz), the variation of harmonic admittances with p have clear patterns. The delay-compensation state indicated by the harmonic admittances can be classified into three cases which are entitled the partial compensation state, the full compensation state, and the over compensation state. The detailed analysis is as follows:

The partial compensation state (p=1 and p=2). Although with p=1 or p=2, the open-loop simplified repetitive predictor can't totally compensate the delay in the grid voltage feedforward loop, but compared with p=0, the harmonic admittances have been effectively reduced, i.e. the impact of distorted grid voltage can be minimized to some extent. And the predictor with p=2 can compensate more delay with better current harmonics minimization capability than that with p=1.

The full compensation state (p=3). When p=3, $G_{OR}(z)$ compensates almost the whole delay in the grid voltage feedforward loop with the minimum harmonic admittances, due to that there are approximately three steps delay in the grid voltage feedforward loop: about one step delay in $G_B(z)$ (analyzed in Section V), one in $G_C(z)$, and one in $G_{PWM}(z)$. In this case, the current harmonics caused by the distorted grid voltage is almost eliminated.

The over compensation state (p=4 or more). As the predictive step p becomes larger than 3, the admittance will increase again. The impact of the distorted grid voltage on the

current harmonics is intensified. It is because that the delayed phase error in the grid voltage feedforward loop is excessively compensated, leading to new advanced phase errors.

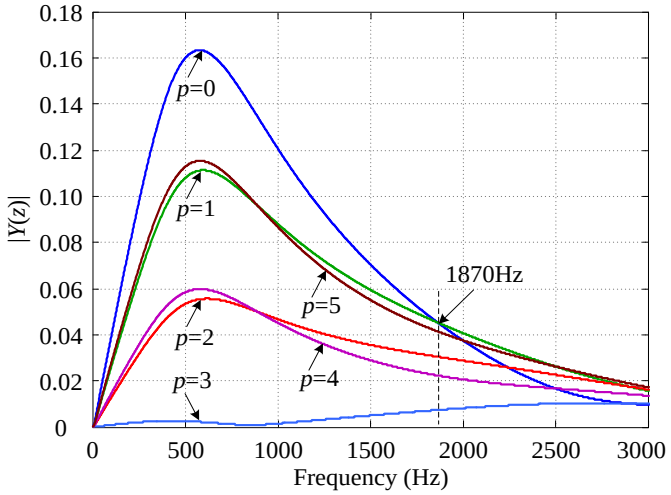

Fig. 18. Admittance-frequency curves with p varying from 0 to 5.

In addition, as shown in Fig. 18, the admittance curve with p=1 is similar to that with p=5, due to they both differ from the full compensation state (p=3) by two steps, p=2 and p=4 as well by one step. Note that the whole delay in the grid voltage feedforward loop may be not the integral multiple of the control period T_c, which makes the full compensation state impossible in certain cases. The value of p making the system in or close to the full compensation state is therefore suggested in these cases.

C. Influence of the Grid Frequency Variation on the Improved Grid Voltage Feedforward Strategy

The impact of grid frequency variation on the improved grid voltage feedforward strategy should be considered. The grid frequency variation will not affect the control delay of the digital controller and the ZOH characteristic of PWM, which are determined by the control period and the switching frequency, respectively. And as seen from the frequency responses of the designed conditioning circuit shown in Fig. 14 (Q=0.707), a slight change in grid frequency has little influence on the phase shift caused by the conditioning circuit. In the grid voltage feedforward loop, the only term affected by the grid frequency variation is the open-loop simplified repetitive predictor, which needs to be further analyzed.

As with the conventional closed-loop repetitive controller/predictor, the open-loop simplified repetitive predictor is also susceptible to grid frequency variation. The predictive error will appear when the sampling frequency is not an integer multiple of the grid frequency. Several solutions used in the classic repetitive controller dealing with the grid frequency variation [45]-[47] can be directly applied to the open-loop simplified repetitive predictor. The common solution for this problem incorporates a real-time adaptive sampling frequency according to the grid frequency variation [45]. Therefore, assuming a situation in which the common solution is adopted and the sampling frequency is adjusted according to the grid frequency variation, the PWM frequency will also change correspondingly since the PWM frequency is half of the sampling frequency. However, the control delay, the delay caused by the ZOH characteristic of PWM, and the period of predictive step are all equal to the sampling period. The control delay and the delay caused by the ZOH characteristic of PWM can still be compensated precisely by the predictor. In addition, the compensation of the delay caused by the conditioning circuit can be comprehended from the perspective of phase shift. With the method of adaptive sampling frequency, the phase shift in one sampling (predictive) period will be a certain value, not varying with the grid frequency variation. Because the grid frequency variation has little influence on the phase shift of the conditioning circuit, the phase shift of the conditioning circuit can also be compensated exactly.

The above analysis shows it is feasible to adopt the existing adaptive sampling frequency method in the improved grid voltage feedforward strategy to deal with the grid frequency variation. It may however increase the computational burden and may lead to the system instability [45]. More detailed study on this issue can be the future work on the basis of this paper.

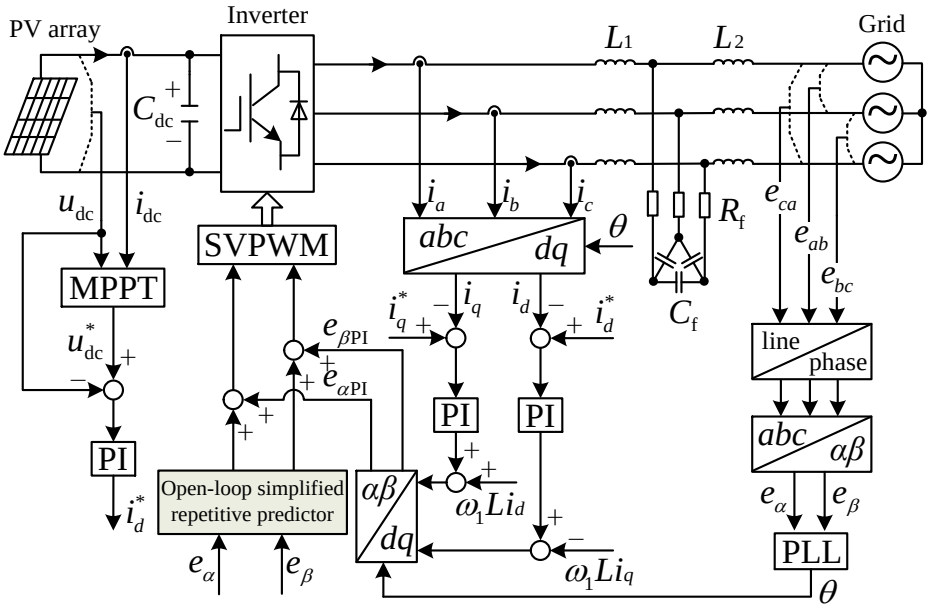

Fig. 19. Scheme of the improved grid voltage feedforward strategy based on the open-loop simplified repetitive predictor.

VII. Experimental Test and Results

In order to test the improved grid voltage feedforward strategy based on the open-loop simplified repetitive predictor, the conventional feedforward decoupling method shown in Fig. 3 is modified to be as shown in Fig. 19. The open-loop simplified repetitive predictor has been inserted to compensate the delay in the grid voltage feedforward loop. Note that Fig. 19 uses e_α and e_β in $\alpha\beta$ coordinate as the feedforward terms instead of e_d and e_q in dq coordinate (the measured values and the real values are not distinguished here). The advantage of using e_α and e_β is that, this has avoided the use of the grid voltage phase angle θ obtained by the phase locked loop (PLL) [48]. The impact of the errors in θ on the feedforward strategy can be therefore eliminated, and one coordinate transformation can be saved. In the outer voltage loop, the dc-link reference voltage u_{dc}^* is obtained by maximum power point tracking (MPPT).

A 250kVA transformerless three-phase grid-connected PV inverter based on the control scheme in Fig. 19 is tested, as shown in Fig. 20. The power generated by the PV array on the two roofs is directly transferred to the grid via the inverter. The system parameters are given in Table II. Note that the MPPT shown in Fig. 19 is disabled and replaced with constant dc-link voltage references for a constant output power of the PV array. Before enabling the PWM when the inverter startups, the control program should run first for several fundamental cycles to obtain the stable grid voltage feedforward term by the open-loop simplified repetitive predictor, as well as waiting for the PLL stable to generate the precision phase angle used for grid voltage oriented vector control.

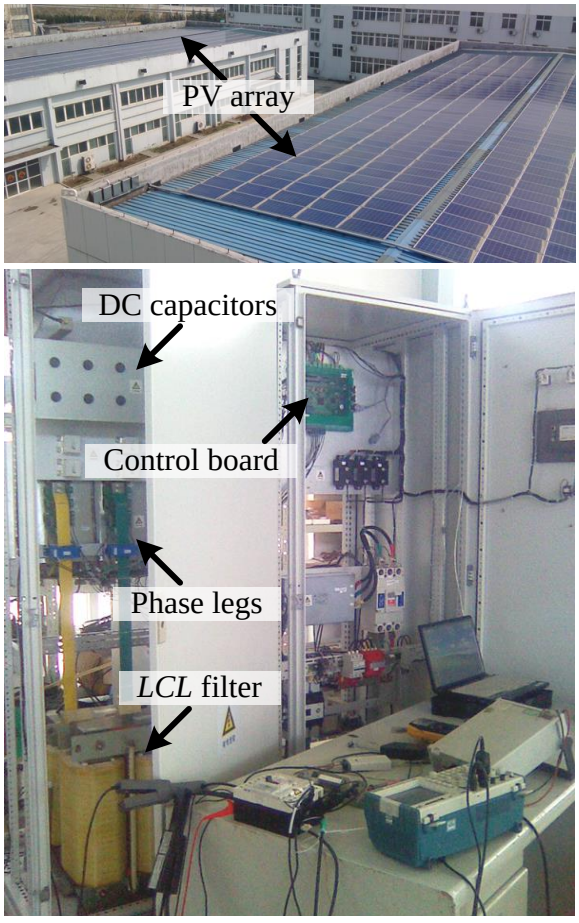

Fig. 20. 250kVA transformerless three-phase grid-connected PV inverter system.

TABLE II
Parameters of the Test System

Symbol	Parameter	Value
S	Rated capacity	250kVA
f_1	Line frequency	50Hz
f_{PWM}	Switching frequency	5kHz
f_s	Sampling frequency	10kHz
T_c	Control period	100μs
C_{dc}	DC-link capacitance	20mF
L_1	Inverter-side inductance	0.22mH
L_2	Grid-side inductance	0.18mH
C_f	Capacitance of *LCL* filter	69μF
R_f	Damping resistor of *LCL* filter	1Ω
K_p	Proportional gain of current loop	0.681
K_i	Integral gain of current loop	17
K_{vp}	Proportional gain of dc-link voltage loop	10
K_{vi}	Integral gain of dc-link voltage loop	800

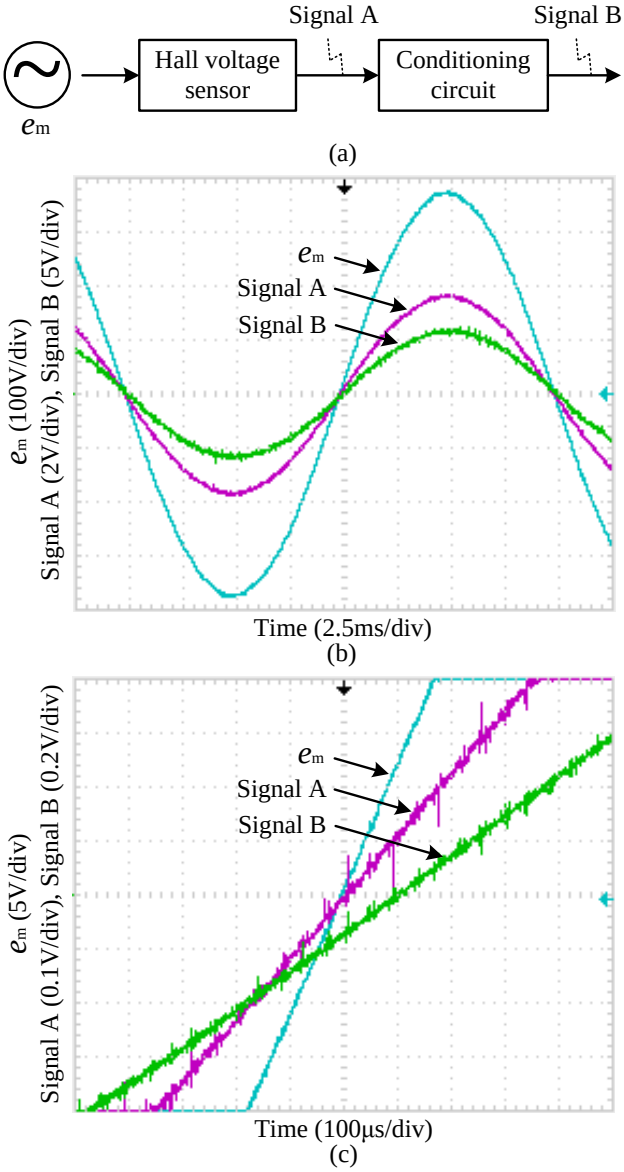

Fig. 21. Delay in the conditioning circuit: (a) the test circuit, (b) measured signals, and (c) zoomed-in zero crossing.

To observe the delay in the designed conditioning circuit, a circuit shown in Fig. 21(a) is tested. The measured ac voltage e_m, Signal A, and Signal B are shown in Fig. 21(b). And Fig. 21(c) shows the zoomed-in zero crossing of Fig. 21(b). As seen, with the negligible delay in the Hall voltage sensor, the zero crossing of e_m almost overlaps that of the Signal A. The zero crossing of Signal B is delayed about 100μs (one step) compared to that of the Signal A, which verifies the correctness of the designed conditioning circuit in Section V.

Fig. 22 shows the program execution flag of 10kHz and the drive signals of 5kHz for IGBTs in Phase A. The flag is low when the digital controller is busy sampling and calculating, and switches to high when spare. The frequencies of the flag and the drive signals are determined by the two synchronous triangle waveforms shown in Fig. 22. The PWM delay of $T_{PWM}/2$ due to the ZOH characteristic and the control delay T_c are clearly shown. And together with Fig. 21, the three-step delays in the grid voltage feedforward loop are verified.

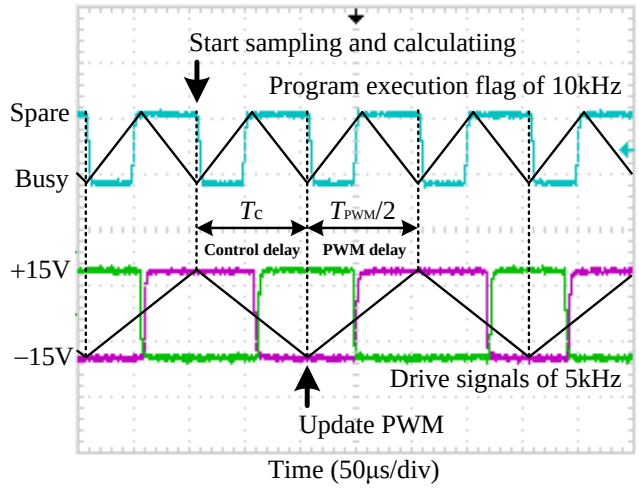

Fig. 22. The PWM delay and the control delay.

During the grid-connected experiments, the grid voltage is slightly distorted, and the harmonics and THD of the three-phase grid voltage measured by the power quality analyzer Fluke 43B are shown in Table III.

TABLE III
HARMONICS AND THD OF THE THREE-PHASE VOLTAGE

Three-phase voltage		Harmonic order				THD
		1	3	5	7	
u_a	Voltage value (V)	233.5	1.3	1.7	3.0	1.9%
	% of fundamental	100%	0.6%	0.7%	1.3%	
u_b	Voltage value (V)	234.7	0.6	1.3	3.2	1.7%
	% of fundamental	100%	0.3%	0.5%	1.4%	
u_c	Voltage value (V)	233.9	1.0	1.2	3.4	1.9%
	% of fundamental	100%	0.4%	0.5%	1.4%	

On the day of experiments, the open-circuit voltage of the PV array which heavily depends on the weather was about 720V. The dc-link voltage reference is set to be the open-circuit voltage of the PV array in order to make the grid side currents i_{ga}, i_{gb}, and i_{gc} zero, i.e. the system is at no-load state. As the grid-side currents equal zero, if the voltage drop on the *LCL* filter is neglected, the output voltage of the inverter should be exactly equal to the grid voltage. As seen in Fig. 19, the reference voltage given to PWM is composed of the feedforward grid voltage and the output of the inner current loop ($e_{\alpha PI}$ and $e_{\beta PI}$). At this time, $e_{\alpha PI}$ and $e_{\beta PI}$ can be taken as the remnant voltage of the grid voltage feedforward loop as stated in Section III. The results of $e_{\alpha PI}$ and $e_{\beta PI}$ with the grid voltage feedforward terms predicted different steps ahead is shown in Fig. 23.

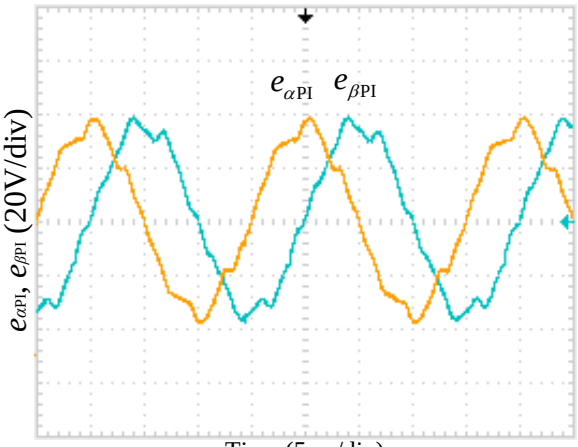

(a)

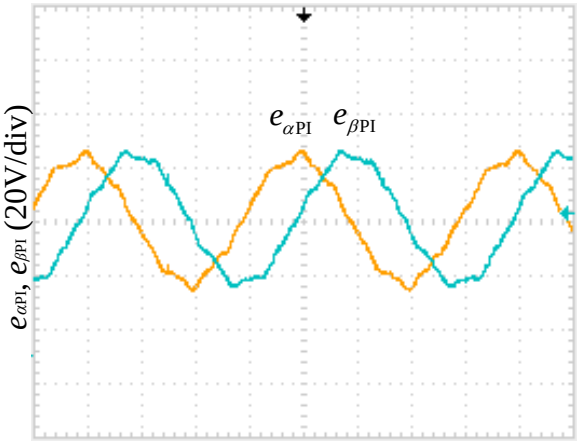

(b)

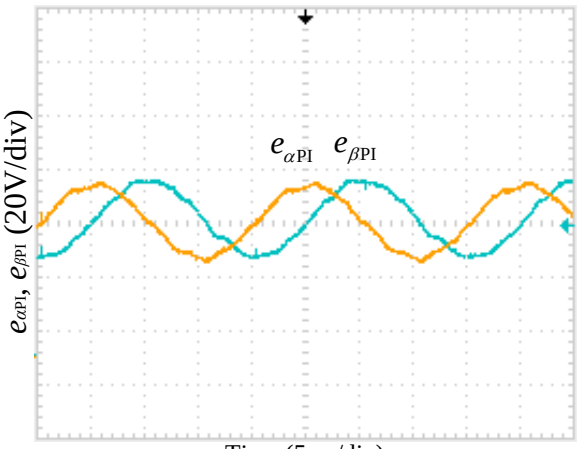

(c)

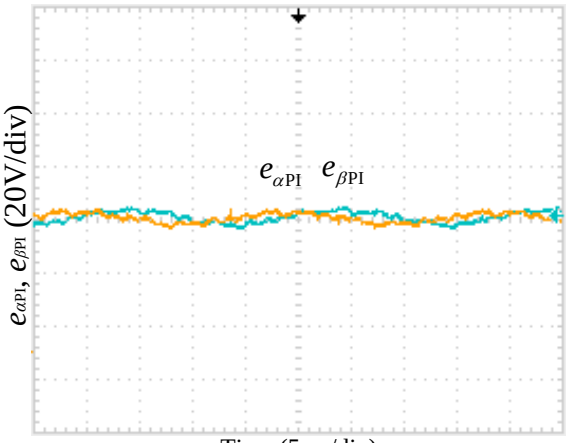

Fig. 23. Waveforms of $e_{\alpha PI}$ and $e_{\beta PI}$ with the grid voltage feedforward terms predicted different steps ahead: (a) p=0, (b) p=1, (c) p=2, and (d) p=3.

As seen in Fig. 23(a), without the open-loop simplified repetitive predictor, $e_{\alpha PI}$ and $e_{\beta PI}$ are heavily distorted with large amplitude, which will lead to harmonics in the output currents. Using the open-loop simplified repetitive predictor, the grid voltage feedforward terms are predicted with different steps ahead (p=1, p=2, and p=3). The results of $e_{\alpha PI}$ and $e_{\beta PI}$ are shown from Fig. 23(b) to Fig. 23(d). As seen, the amplitude and distortion of $e_{\alpha PI}$ and $e_{\beta PI}$ are gradually decreased with the increasing predictive steps. When p=3, the amplitude and distortion of $e_{\alpha PI}$ and $e_{\beta PI}$ are the smallest. The results match well with the analysis in Section VI about the delay-compensation, and prove that with p=3, the grid voltage feedforward loop is in or close to the full compensation state in the test system.

Fig. 24 shows the experimental results with the conventional and the improved grid voltage feedforward strategies. The output power of the inverter is 28kW. As seen in Fig. 24(a), using the conventional grid voltage feedforward strategy, due to the heavily distorted remnant voltage shown in Fig. 23(a), the three-phase currents are distorted heavily due to harmonics. Under the same grid condition, the same control strategy has been applied on a 10kVA PV inverter with the filtering inductor of 2.7mH. In contrast, only slight distortion appears in the three-phase currents. It is indicated that the high power inverters with smaller filtering inductor is more susceptible to the slightly-distorted grid voltage. Fig. 24(b) shows the results when applying the improved grid voltage feedforward strategy with the feedforward term predicted 3 steps ahead, the quality of the three-phase currents are significantly improved.

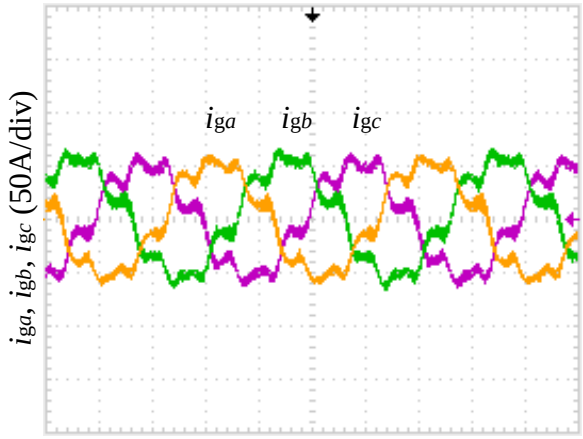

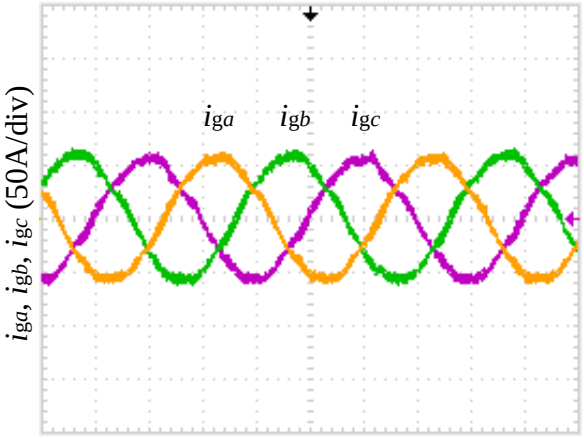

Fig. 24. Waveforms of the three-phase currents: (a) with the conventional grid voltage feedforward strategy, and (b) with the improved grid voltage feedforward strategy.

Table IV and Table V further show the harmonics and THD of the currents in Fig. 24. Comparing each order harmonic in the two tables, it is found that all the low order harmonics are minimized effectively with the improved grid voltage feedforward strategy. The results match well with the analysis of harmonic admittances shown in Fig. 18, which can be taken as the reflex of the current harmonics minimization capability.

TABLE IV
HARMONICS AND THD OF THE THREE-PHASE CURRENTS WITH **CONVENTIONAL** GRID VOLTAGE FEEDFORWARD STRATEGY

Three-phase currents		Harmonic order				THD
		1	3	5	7	
i_{ga}	Current value (A)	39.41	1.22	3.53	5.49	17.6%
	% of fundamental	100%	3.1%	9.1%	14.1%	
i_{gb}	Current value (A)	40.41	0.30	3.04	7.57	21.1%
	% of fundamental	100%	0.8%	7.7%	19.1%	
i_{gc}	Current value (A)	39.41	0.37	3.55	7.48	19.5%
	% of fundamental	100%	1.0%	9.2%	16.7%	

TABLE V
HARMONICS AND THD OF THE THREE-PHASE CURRENTS WITH **IMPROVED** GRID VOLTAGE FEEDFORWARD STRATEGY

Three-phase currents		Harmonic order				THD
		1	3	5	7	
i_{ga}	Current value (A)	38.66	0.68	0.61	0.76	3.5%
	% of fundamental	100%	1.8%	1.6%	2.0%	
i_{gb}	Current value (A)	39.79	0.18	0.64	0.75	3.2%
	% of fundamental	100%	0.4%	1.6%	1.9%	
i_{gc}	Current value (A)	38.66	0.15	0.86	0.93	3.6%
	% of fundamental	100%	0.4%	1.7%	2.4%	

Then, the output power of the inverter is increased to 44kW. With the two strategies, the voltage and current of Phase A are shown in Fig. 25. The THD of the currents are 8.5% and 2.8%, respectively. As seen in Fig. 25(a), with the increased output power, the current quality with the conventional grid voltage feedforward strategy is improved, but still unacceptable. In

contrast, the current in Fig. 25(b) with the improved grid voltage feedforward strategy is further improved and satisfying.

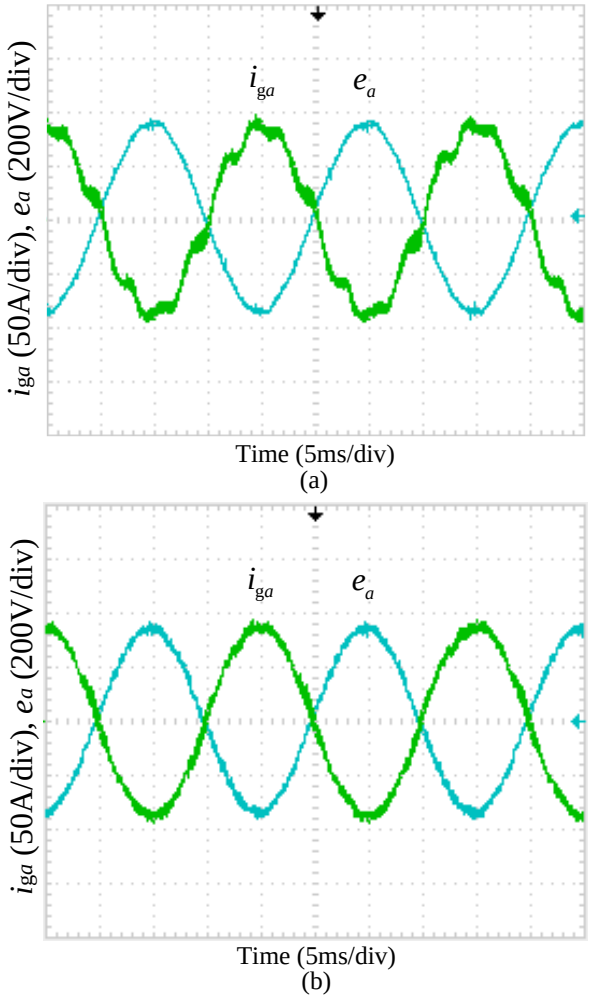

Fig. 25. Waveforms of voltage and current in Phase A: (a) with the conventional grid voltage feedforward strategy, and (b) with the improved grid voltage feedforward strategy.

Another benefits of using the proposed improved feedforward strategy is the suppression of the starting currents, which may trigger the system protection or even damage the devices. In PV systems, to lower the starting currents, the dc-link voltage is usually set to be the open-circuit voltage of the PV array when the inverter starts. And then by MPPT, the dc-link voltage is regulated gradually to the maximum power point. Fig. 26 shows the comparison of the starting currents with the two feedforward strategies. As seen in Fig. 26(a), with the conventional grid voltage feedforward strategy, very large starting currents appear. After applying the improved grid voltage feedforward strategy, the starting currents in Fig. 26(b) almost disappear. This phenomenon can be explained as follows. Neglecting the voltage drop on *LCL* filter, ideally, the inverter output voltage should be exactly equal to the grid voltage at no-load state. And it should be easy to realize with grid voltage feedforward. However, due to the errors in the grid voltage feedforward loop, there is large remnant voltage after the feedforward, as shown in Fig. 23(a). And the remnant voltage needs to be compensated by the PI controllers in current loops. Moreover, when the system starts, the initial outputs of the PI controllers in current loops are zero. It takes some time for the PI controllers to generate the large compensation voltage, leading to the large starting currents in Fig. 26(a). After applying the open-loop simplified repetitive controller, the remnant voltage is dramatically decreased, as seen in Fig. 23(d), which eases the burden on the PI controllers in current loops leading a smooth start. In addition, it should be noted that the currents before start in Fig. 26 are not zero, owing to that the grid voltage generates currents flowing through the capacitors of the *LCL* filter.

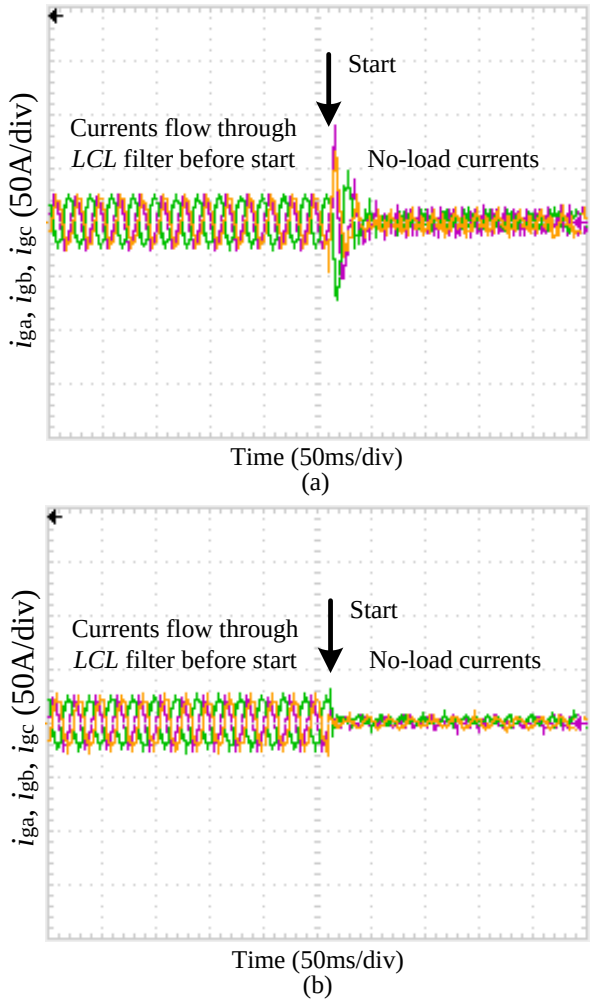

Fig. 26. Starting currents: (a) with the conventional grid voltage feedforward strategy, and (b) with the improved grid voltage feedforward strategy.

The proposed strategy with the simplified predictor has also been tested under other non-ideal grid conditions. Regarding the unbalanced grid voltage, if only the fundamental voltage is considered, it can cause double frequency (e.g. 100Hz for 50Hz grid) power pulsation on both ac and dc side of the inverter. This issue is different from the delay problem concerned in this paper and therefore will not affect the design of the feedforward strategy. Through simulation it has been found that the improved grid voltage feedforward strategy works well under unbalanced grid voltage but it cannot help with the situation, e.g. attenuating the power ripple, etc.

Further, the simulation with a sudden dip of 10% in three-phase grid voltage is carried out to test the performance of the proposed strategy under grid voltage perturbations, the three-phase currents are shown in Fig. 27. As seen, with the conventional grid voltage feedforward strategy, current overshoot happens at the transient of voltage dip. Meanwhile, with the improved grid voltage feedforward strategy, besides

this current overshoot at the transient of voltage dip, another obvious current distortion appears after one fundamental period due to the fact that the repetitive predictor relies on the former input values. Given the improvement of the current waveforms in steady state, this transient current distortion caused by grid voltage dip can be acceptable.

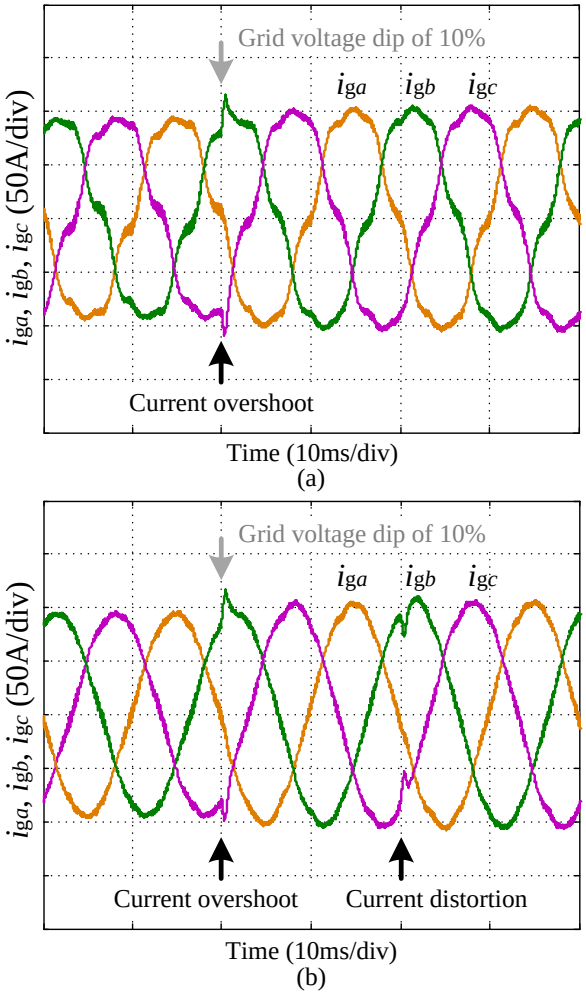

Fig. 27. Simulation results at grid voltage dip of 10%: (a) with the conventional grid voltage feedforward strategy, and (b) with the improved grid voltage feedforward strategy.

VIII. Conclusions

Grid voltage feedforward strategy is the most direct solution for grid-connected inverters dealing with the condition of distorted grid voltage. However, its performance is dramatically decreased by the delays in the grid voltage feedforward loop, especially for high-power inverters with low switching frequency and low filtering inductance. The delays mainly include the phase shift caused by the conditioning circuit, the control delay of the digital controller, and the ZOH characteristic of PWM. An improved grid voltage feedforward strategy has been proposed with enhanced feedforward precision by the open-loop simplified repetitive predictor and the carefully designed conditioning circuit. The experimental results on a 250VA solar power generation system have validated that, with the predictive steps making the grid voltage feedforward loop in or close to the full compensation state, the improved grid voltage feedforward strategy can effectively attenuate the current harmonics caused by the distorted grid voltage as well as the starting currents.

Although the improved feedforward strategy is analyzed based on a PV inverter, it can also be applied to other grid-connected converter control systems conveniently.

References

[1] K. D. McBee and M. G. Simoes, "Evaluating the long-term impact of a continuously increasing harmonic demand on feeder-level voltage distortion," *IEEE Trans. Ind. Appl.*, vol. 50, no. 3, pp. 2142-2149, May/Jun. 2014.

[2] M. Liserre, R. Teodorescu, and F. Blaabjerg, "Stability of photovoltaic and wind turbine grid-connected inverters for a large set of grid impedance values," *IEEE Trans. Power Electron.*, vol. 21, no. 1, pp. 263-272, Jan. 2006.

[3] T. Abeyasekera, C. M. Johnson, D. J. Atkinson, and M. Armstrong, "Suppression of line voltage related distortion in current controlled grid connected inverters," *IEEE Trans. Power Electron.*, vol. 20, no. 6, pp. 1393-1401, Nov. 2005.

[4] E. Twining and D. G. Holmes, "Grid current regulation of a three-phase voltage source inverter with an *LCL* input filter," *IEEE Trans. Power Electron.*, vol. 18, no. 3, pp. 888-895, May 2003.

[5] P. Xiao, K. A. Corzine, and G. K. Venayagamoorthy, "Multiple reference frame-based control of three-phase PWM boost rectifiers under unbalanced and distorted input conditions," *IEEE Trans. Power Electron.*, vol. 23, no. 4, pp. 2006-2017, Jul. 2008.

[6] X. Yuan, W. Merk, H. Stemmler, and J. Allmeling, "Stationary-frame generalized integrators for current control of active power filters with zero steady-state error for current harmonics of concern under unbalanced and distorted operating conditions," *IEEE Trans. Ind. Appl.*, vol. 38, no. 2, pp. 523-532, Mar. 2002.

[7] C. Lascu, L. Asiminoaei, I. Boldea, and F. Blaabjerg, "High performance current controller for selective harmonic compensation in active power filters," *IEEE Trans. Power Electron.*, vol. 22, no. 5, pp. 1826-1835, Sep. 2007.

[8] C. Lascu, L. Asiminoaei, I. Boldea, and F. Blaabjerg, "Frequency response analysis of current controllers for selective harmonic compensation in active power filters," *IEEE Trans. Ind. Electron.*, vol. 56, no. 2, pp. 337-347, Feb. 2009.

[9] D. N. Zmood and D. G. Holmes, "Stationary frame current regulation of PWM inverters with zero steady-state error," *IEEE Trans. Power Electron.*, vol. 18, no. 3, pp. 814-822, May 2003.

[10] H. Xu, J. Hu, and Y. He, "Operation of wind-turbine-driven DFIG systems under distorted grid voltage conditions: analysis and experimental validations," *IEEE Trans. Power Electron.*, vol. 27, no. 5, pp. 2354-2366, May 2012.

[11] H. Nian and Y. Song, "Direct power control of doubly fed induction generator under distorted grid voltage," *IEEE Trans. Power Electron.*, vol. 29, no. 2, pp. 894-905, Feb. 2014.

[12] F. Gonzalez-Espin, G. Garcera, I. Patrao, and E. Figueres, "An adaptive control system for three-phase photovoltaic inverters working in a polluted and variable frequency electric grid," *IEEE Trans. Power Electron.*, vol. 27, no. 10, pp. 4248-4261, Oct. 2012.

[13] J. Gao, T. Q. Zheng, and F. Lin, "Improved deadbeat current controller with a repetitive-control-based observer for PWM rectifiers," *J. Power Electron.*, vol. 11, no. 1, pp. 64-73, Jan. 2011.

[14] Q.-N. Trinh and H.-H. Lee, "An enhanced grid current compensator for grid-connected distributed generation under nonlinear loads and grid voltage distortions," *IEEE Trans. Ind. Electron.*, vol. 61, no. 12, pp. 6528-6537, Dec. 2014.

[15] Z. Yao and L. Xiao, "Control of single-phase grid-connected inverters with nonlinear loads," *IEEE Trans. Ind. Electron.*, vol. 60, no. 4, pp. 1384-1389, Apr. 2013.

[16] Z. Liu, J. Liu, and Y. Zhao, "A unified control strategy for three-phase inverter in distributed generation," *IEEE Trans. Power Electron.*, vol. 29, no. 3, pp. 1176-1191, Mar. 2014.

[17] Y. Tao, Q. Liu, Y. Deng, X. Liu, and X. He, "Analysis and mitigation of inverter output impedance impacts for distributed energy resource interface," *IEEE Trans. Power Electron.*, vol. 30, no. 7, pp. 3563-3576, Jul. 2015.

[18] X. Wang, X. Ruan, S. Liu, and C. K. Tse, "Full feedforward of grid voltage for grid-connected inverter with *LCL* filter to suppress current distortion due to grid voltage harmonics," *IEEE Trans. Power Electron.*, vol. 25, no. 12, pp. 3119-3127, Dec. 2010.

[19] W. Li, D. Pan, X. Ruan, and X. Wang, "A full-feedforward scheme of grid voltages for a three-phase grid-connected inverter with an *LCL* filter," in

Proc. Energy Convers. Congr. and Expo., Phoenix, AZ, Sep. 2011, pp. 96-103.

[20] W. Li, X. Ruan, D. Pan, and X. Wang, "Full-feedforward schemes of grid voltages for a three-phase *LCL*-type grid-connected inverter," *IEEE Trans. Ind. Electron.*, vol. 60, no. 6, pp. 2237-2250, Jun. 2013.

[21] M. Xue, Y. Zhang, Y. Kang, Y. Yi, S. Li, and F. Liu, "Full feedforward of grid voltage for discrete state feedback controlled grid-connected inverter with *LCL* filter," *IEEE Trans. Power Electron.*, vol. 27, no. 10, pp. 4234-4247, Oct. 2012.

[22] J. Xu, S. Xie, and T. Tang, "Improved control strategy with grid-voltage feedforward for *LCL*-filter-based inverter connected to weak grid," *IET Power Electron.*, vol. 7, no. 10, pp. 2660-2671, Oct. 2014.

[23] J. R. Fischer, S. A. Gonzalez, M. A. Herran, M. G. Judewicz, and D. O. Carrica, "Calculation-delay tolerant predictive current controller for three-phase inverters," *IEEE Trans. Ind. Inf.*, vol. 10, no. 1, pp. 233-242, Feb. 2014.

[24] T.-V. Tran, T.-W. Chun, H.-H. Lee, H.-G. Kim, and E.-C. Nho, "Control method for reducing the THD of grid current of three-phase grid-connected inverters under distorted grid voltages," *J. Power Electron.*, vol. 13, no. 4, pp. 712-718, Jul. 2013.

[25] Y. He, J. Liu, J. Tang, Z. Wang, and Y. Zou, "Deadbeat control with a repetitive predictor for three-level active power filters," *J. Power Electron.*, vol. 11, no. 4, pp. 583-590, Jul. 2011.

[26] H. Ouyang, K. Zhang, P. Zhang, Y. Kang, and J. Xiong, "Repetitive compensation of fluctuating DC link voltage for railway traction drives," *IEEE Trans. Power Electron.*, vol. 26, no. 8, pp. 2160-2171, Aug. 2011.

[27] S. Jiang, D. Cao, Y. Li, J. Liu, and F. Peng, "Low-THD, fast-transient, and cost-effective synchronous-frame repetitive controller for three-phase UPS inverters," *IEEE Trans. Power Electron.*, vol. 27, no. 6, pp. 2994-3005, Jun. 2012.

[28] L. Thede, *Practical Analog and Digital Filter Design*, 3rd ed. Norwood, MA, USA: Artech House, 2004, pp. 87–92, ch. 4, sec. 2.

[29] G. S. Moschytz, "Low-sensitivity, low-power active-RC allpole filters using impedance tapering," *IEEE Trans. Circuits Syst. II, Analog Digit. Signal Process. (1993-2003)*, vol. 46, no. 8, pp. 1009-1026, Aug. 1999.

[30] M. Liserre, F. Blaabjerg, and S. Hansen, "Design and control of an *LCL*-filter-based three-phase active rectifier," *IEEE Trans. Ind. Appl.*, vol. 41, no. 5, pp. 1281-1291, Sep. 2005.

[31] C. Wan, M. Huang, C.K. Tse, S.-C. Wong, and X. Ruan, "Nonlinear behavior and instability in a three-phase boost rectifier connected to a nonideal power grid with an interacting load," *IEEE Trans. Power Electron.*, vol. 28, no. 7, pp. 3255-3265, Jul. 2013.

[32] B. Bahrani, A. Karimi, B. Rey, and A. Rufer, "Decoupled dq-current control of grid-tied voltage source converters using nonparametric models," *IEEE Trans. Ind. Electron.*, vol. 60, no. 4, pp. 1356-1366, Apr. 2013.

[33] V. Blasko and V. Kaura, "A new mathematical model and control of a three-phase AC-DC voltage source converter," *IEEE Trans. Power Electron.*, vol. 12, no. 1, pp. 116-123, Jan. 1997.

[34] S. Ziegler, R. C. Woodward, H. H. C. Iu, and L. J. Borle, "Current sensing techniques: a review," *IEEE Sensors J.*, vol. 9, no. 4, pp. 354-376, Apr. 2009.

[35] J. L. Agorreta, M. Borrega, J. López, and L. Marroyo, "Modeling and control of *N*-paralleled grid-connected inverters with *LCL* filter coupled due to grid impedance in PV plants," *IEEE Trans. Power Electron.*, vol. 26, no. 3, pp. 770-785, Mar. 2011.

[36] E. Wu and P. W. Lehn, "Digital current control of a voltage source converter with active damping of *LCL* resonance," *IEEE Trans. Power Electron.*, vol. 21, no. 5, pp. 1364-1373, Sep. 2006.

[37] X. Zhang and J. W. Spencer, "Study of multisampled multilevel inverters to improve control performance," *IEEE Trans. Power Electron.*, vol. 27, no. 11, pp. 4409-4416, Nov. 2012.

[38] S.-H. Hwang and J.-M. Kim, "Dead time compensation method for voltage-fed PWM inverter," *IEEE Trans. Energy Convers.*, vol. 25, no. 1, pp. 1-10, Mar. 2010.

[39] Y. Yang, F. Blaabjerg, and H. Wang, "Low-voltage ride-through of single-phase transformerless photovoltaic inverters," *IEEE Trans. Ind. Appl.*, vol. 50, no. 3, pp. 1942-1952, May/Jun. 2014.

[40] O. Bretscher, *Linear Algebra with Applications*, 4th ed. Upper Saddle River, NJ, USA: Pearson, 2009, pp. 220–232, ch. 5, sec. 4.

[41] A. G. Yepes, F. D. Freijedo, J. Doval-Gandoy, O. López, J. Malvar, and P. Fernandez-Comesaña, "Effects of discretization methods on the performance of resonant controllers," *IEEE Trans. Power Electron.*, vol. 25, no. 7, pp. 1692-1712, Jul. 2010.

[42] F. Briz, M. W. Degner, and R. D. Lorenz, "Analysis and design of current regulators using complex vectors," *IEEE Trans. Ind. Appl.*, vol. 36, no. 3, pp. 817-825, May/Jun. 2000.

[43] Y. A.-R. I. Mohamed, "Suppression of low- and high-frequency instabilities and grid-induced disturbances in distributed generation inverters," *IEEE Trans. Power Electron.*, vol. 26, no. 12, pp. 3790-3803, Dec. 2011.

[44] G. Ellis, *Control System Design Guide*, 3rd ed. San Diego, CA, USA: Academic, 2004, pp. 40-45, ch. 3, sec. 4.

[45] M. A. Herrán, J. R. Fischer, S. A. González, M. G. Judewicz, I. Carugati, and D. O. Carrica, "Repetitive control with adaptive sampling frequency for wind power generation systems," *IEEE J. Emerg. Sel. Topics Power Electron.*, vol. 2, no. 1, pp. 58-69, Mar. 2014.

[46] J. M. Olm, G. A. Ramos, and R. Costa-Castelló, "Stability analysis of digital repetitive control systems under time-varying sampling period," *IET Control Theory & Appl.*, vol. 5, no. 1, pp. 29-37, Jan. 2011.

[47] D. Chen, J. Zhang, and Z. Qian, "An improved repetitive control scheme for grid-connected inverter with frequency-adaptive capability," *IEEE Trans. Ind. Electron.*, vol. 60, no. 2, pp. 814-823, Feb. 2013.

[48] V. Kaura and V. Blasko, "Operation of a phase locked loop system under distorted utility conditions," *IEEE Trans. Ind. Appl.*, vol. 33, no. 1, pp. 58-63, Jan./Feb. 1997.